



OPEN

## Influence of the modifiers in polyol method on magnetically induced hyperthermia and biocompatibility of ultrafine magnetite nanoparticles

Adrian Radoń<sup>1,2</sup>✉, Agnieszka Włodarczyk<sup>3</sup>, Łukasz Sieroń<sup>3</sup>, Magdalena Rost-Roszkowska<sup>4</sup>, Łukasz Chajec<sup>4</sup>, Dariusz Łukowiec<sup>1</sup>, Agnieszka Ciuraszkiewicz<sup>2</sup>, Piotr Gębara<sup>5</sup>, Stanisław Wacławek<sup>6</sup> & Aleksandra Kolano-Burian<sup>2</sup>

Magnetite nanoparticles (Fe<sub>3</sub>O<sub>4</sub> NPs) are widely tested in various biomedical applications, including magnetically induced hyperthermia. In this study, the influence of the modifiers, i.e., urotropine, polyethylene glycol, and NH<sub>4</sub>HCO<sub>3</sub>, on the size, morphology, magnetically induced hyperthermia effect, and biocompatibility were tested for Fe<sub>3</sub>O<sub>4</sub> NPs synthesized by polyol method. The nanoparticles were characterized by a spherical shape and similar size of around 10 nm. At the same time, their surface is functionalized by triethylene glycol or polyethylene glycol, depending on the modifiers. The Fe<sub>3</sub>O<sub>4</sub> NPs synthesized in the presence of urotropine had the highest colloidal stability related to the high positive value of zeta potential (26.03 ± 0.55 mV) but were characterized by the lowest specific absorption rate (SAR) and intrinsic loss power (ILP). The highest potential in the hyperthermia applications have NPs synthesized using NH<sub>4</sub>HCO<sub>3</sub>, for which SAR and ILP were equal to 69.6 ± 5.2 W/g and 0.613 ± 0.051 nHm<sup>2</sup>/kg, respectively. Their application possibility was confirmed for a wide range of magnetic fields and by cytotoxicity tests. The absence of differences in toxicity to dermal fibroblasts between all studied NPs was confirmed. Additionally, no significant changes in the ultrastructure of fibroblast cells were observed apart from the gradual increase in the number of autophagous structures.

Magnetite nanoparticles are one of the most promising nanomaterials in medical applications according to their unique physicochemical properties and biocompatibility<sup>1,2</sup>. Additionally, Fe<sub>3</sub>O<sub>4</sub> NPs can be synthesized in various sizes, shapes and in the form of core-shell structures, in which shells can be inorganic or polymer-based<sup>3-5</sup>. The many synthesis methods and modification protocols were proposed in the literature to synthesize even multifunctional platforms dedicated to nanomedicine. Furthermore, various factors, not only morphological ones, such as doping and surface functionalization, change the properties and modify the range of applicability of magnetite nanoparticles. Despite their possible use in medicine as MRI contrast, drug delivery systems, anticancer agents, and hyperthermia<sup>6,7</sup>, their application range is much broader and includes catalysis<sup>8</sup>, heavy metals adsorption<sup>9</sup>, microwave absorption<sup>10</sup>, and supercapacitors<sup>11</sup>.

Modifying magnetite nanoparticles' morphology and surface chemical composition can be performed during the synthesis stage and afterward. Roca et al.<sup>3</sup> have shown that the shape of the nanoparticles can be controlled in a few ways, including modifying the iron source precursors and using selected organic modifiers. Moreover,

<sup>1</sup>Faculty of Mechanical Engineering, Silesian University of Technology, Konarskiego 18 a St., 44-100 Gliwice, Poland. <sup>2</sup>Łukasiewicz Research Network - Institute of Non-Ferrous Metals, Sowinskiego 5 St., 44-100 Gliwice, Poland. <sup>3</sup>Department of Medical Genetics, Faculty of Medical Sciences in Katowice, Medical University of Silesia, Medyków 18, 40-752 Katowice, Poland. <sup>4</sup>Institute of Biology, Biotechnology and Environmental Protection, University of Silesia in Katowice, Bankowa 9, 40-007 Katowice, Poland. <sup>5</sup>Department of Physics, Częstochowa University of Technology, Armii Krajowej 19, 42-200 Częstochowa, Poland. <sup>6</sup>Institute for Nanomaterials, Advanced Technologies and Innovation, Technical University of Liberec, Studentská 1402/2, 461 17 Liberec 1, Czech Republic. ✉email: adrian.radon@imn.lukasiewicz.gov.pl

the size and spontaneous functionalization of the magnetite nanoparticle surface can be controlled in the co-precipitation method by using various organic modifiers such as dextrin and organic acids (tartaric and citric ones)<sup>12</sup>. While the shape and size of Fe<sub>3</sub>O<sub>4</sub> NPs influence both biocompatibility and magnetically induced hyperthermia effect, the functionalization of their surface allows the synthesis of hydrophobic or hydrophilic nanoparticles<sup>13–16</sup>. Generally, magnetite nanoparticles should be hydrophilic in biomedical applications to form a stable water-based dispersion. To achieve that, the magnetite surface can be refunctionalized, or co-precipitation and polyol methods should be chosen to synthesize nanoparticles with high colloidal stability<sup>17–19</sup>. While the co-precipitation method is one of the most studied ones with high synthesis yield, the prepared nanoparticles are agglomerated, and their size distribution is wide. Accordingly, the polyol method is most promising in biomedical applications. In this case surface of nanoparticles can be functionalized by the reducing solvent<sup>19</sup> or by introducing into the reaction solution organic modifiers such as ethylenediamine, (3-aminopropyl) triethoxysilane, and citric acid<sup>20–22</sup>. Functionalized magnetite nanoparticles can be used then as MRI contrast or as the agent in magnetically induced hyperthermia.

Magnetic NPs show great potential for biomedical applications<sup>23</sup>. One of them is the induction of local hyperthermia to destroy a particular type of cells and tissues. In this case, magnetite nanoparticles can be used as an agent for targeted therapy, in which NPs are introduced into the tumor and hyperthermia is induced to destroy these tumor cells while other organs and tissues remain intact<sup>24</sup>. Compared to broadly used chemotherapy with many severe side effects, this is a significant advantage. However, for them to be efficiently used in anticancer therapy, NPs should possess two main properties. One is the ability to induce hyperthermia strong enough to kill tumor cells in response to magnetic stimuli, and second, their use should be safe and cause no other side effects.

Unfortunately, due to their small size, NPs can potentially appear toxic to healthy cells and tissues where hyperthermia is not induced<sup>25</sup>. Moreover, in the presence of enzymes in biological structures, NPs can undergo chemical and structural changes that alter their biological properties<sup>26</sup>. Thus their toxic effect can appear later and affect tissues sometimes after treatment. Therefore, it is essential to synthesize NPs as less toxic as possible. Many factors influence NPs toxicity, such as composition, size, aggregate tendency, and surface modification<sup>25,26</sup>. Coating with organic and nonorganic compounds such as polyethylene glycol and polyvinyl alcohol is the most common modification of NPs that decreases their toxicity<sup>27</sup>. This modification prevents the aggregation of NPs and protects them from interaction with proteins, enzymes, and other cell compounds<sup>28</sup>. Another type of modification is functionalization to give them appropriate chemical and physical properties, e.g., electric charge<sup>27</sup>. Also, combination with organic compounds or proteins affects NPs internalization and toxicity<sup>29</sup>. Moreover, coupling with proteins can give them affinity to particular types of cells (desirable for NP-mediated targeted drug delivery) or increase their biocompatibility<sup>30</sup>.

The literature shows that magnetite nanoparticles show low cytotoxicity on human fibroblasts<sup>31</sup>; however, treatment of patients with magnetite nanoparticles may undoubtedly have a negative impact on some cells and lead to the development of diseases such as Parkinson's disease, Alzheimer's disease<sup>32,33</sup> or cardiovascular diseases<sup>34</sup>. It is known that the cytotoxicity of nanoparticles depends on aggregation rate, environmental conditions, size of nanoparticles, shape, concentration, proportion, and type of polymers used to form the shell<sup>33</sup>. Therefore, researches on nanoparticles are crucial to improve their performance without losing their biocompatibility, thus minimizing the possibility of developing diseases related to their use during treatment. Accordingly, in this study, ultrafine magnetite nanoparticles with a size of about 10 nm and modified surface were synthesized using the polyol method. Organic (polyethylene glycol, hexamethylenetetramine) and inorganic (ammonium bicarbonate) modifiers were added to determine the role of the synthesis method and modification on the surface chemistry and magnetically induced hyperthermia effect. While polyethylene glycols with various molecular weights are widely tested in the synthesis of magnetite nanoparticles dedicated to biomedical applications, ammonium bicarbonate and hexamethylenetetramine were not yet tested in this field; however, some of the works confirm their role in the synthesis of magnetite nanoparticles (especially using hydrothermal route) with unique morphology and properties<sup>35–38</sup>. Accordingly, the role of these modifiers on the size and colloidal stability was examined, together with the possibility of applying magnetite nanoparticles in cyclic hyperthermia treatment, which could be an interesting approach in the controlled drug delivery process in anticancer treatment. Furthermore, their toxicity to human fibroblast cells in vitro was tested and discussed in the context of the applied synthesis modifications.

## Materials and methods

**Magnetite nanoparticles synthesis.** Magnetite nanoparticles were synthesized using the polyol method and polyethylene glycol 600 (PEG), urotropine (hexamethylenetetramine), and NH<sub>4</sub>HCO<sub>3</sub> as modifiers. The synthesized samples were marked as Fe<sub>3</sub>O<sub>4</sub>–PEG, Fe<sub>3</sub>O<sub>4</sub>–URO, and Fe<sub>3</sub>O<sub>4</sub>–NH<sub>4</sub>HCO<sub>3</sub>, respectively. To synthesize Fe<sub>3</sub>O<sub>4</sub>–URO and Fe<sub>3</sub>O<sub>4</sub>–NH<sub>4</sub>HCO<sub>3</sub> nanoparticles, five mmol of Fe(acac)<sub>3</sub> was dissolved in 100 ml of triethylene glycol (TREG). Afterward, two mmol of hexamethylenetetramine or NH<sub>4</sub>HCO<sub>3</sub> was added to the solution and heated to 271 °C. The synthesis was carried out in 30 min. Next, the product was cooled to room temperature, and 100 ml of ethyl acetate was added to precipitate ultrafine nanoparticles. Finally, the black product was removed from the post-reaction solution using a magnetic field and washed thrice with ethyl acetate. A similar procedure was applied to obtain Fe<sub>3</sub>O<sub>4</sub>–PEG nanoparticles. In this case, synthesis was performed using PEG and TREG (25:75 ml, respectively) without adding other modifiers. The synthesized nanoparticles, for further characterization, were stored in ethyl acetate. Before all tests, nanoparticles were removed from the ethyl acetate using a magnetic field. Afterwards, samples were washed with the DI water three times and dried at 60 °C to ensure that ethyl acetate was not presented in dispersions dedicated to the magnetic hyperthermia and cytotoxicity measurements.

**Structure characterization.** The structure and phase purity of synthesized samples were analyzed using the X-ray diffraction method. The investigation was carried out on a Rigaku MiniFlex 600 (Rigaku Corporation, Tokyo, Japan) diffractometer equipped with copper tube Cu K $\alpha$  ( $\lambda = 0.15406$  nm) as a radiation source (tube voltage 40 kV, current 15 mA). The scan step width was 0.02° in the scan range from 20° to 90° of the 2 $\theta$  scale. The morphology and structure of synthesized samples were determined using a transmission electron microscope (TEM) S/TEM TITAN 80–300 (FEI Company, Eindhoven, The Netherlands). For this purpose, a few milligrams of the synthesized nanoparticles were sonicated in ultrapure ethanol to obtain stable dispersion. Afterward, one drop of this dispersion was placed on the copper grid with a carbon film.

The average size of nanoparticles ( $D_{\text{TEM}}$ , as mean value) was measured for at least 100 different nanoparticles and at least three different micrographs. In addition, the presence of the modifiers on the surface of nanoparticles was determined using infrared spectroscopy. Fourier-transform infrared (FTIR) spectra were measured for magnetite nanoparticles using the KBr pellet method in infrared transmission mode using a Nicolet 6700/8700 FTIR spectrometer (Thermo Fisher Scientific, Waltham, MA, USA). Magnetic properties were characterized using a vibrating-sample magnetometer LakeShore VSM 7307 at room temperature and in a magnetic field up to 10 kOe. The colloidal stability tests were performed for the water dispersions with 3 mg/ml concentration and 10 mg/ml. For this purpose, the washed and dried magnetite nanoparticles were sonicated with DI water using a UP200St device (26 kHz, 10 W) in a pulse mode. The zeta potential and average size distribution of dispersed particles were analyzed by a Zetasizer Nano ZS (Malvern PANalytical Ltd, United Kingdom) with an autocorrelation function of 10 s and at room temperature. Samples were measured in triplicate. The standard parameters for the characterization of Fe<sub>3</sub>O<sub>4</sub> (refractive index = 2 and absorbance = 0.01) were chosen.

**Magnetic hyperthermia measurements.** The magnetically induced hyperthermia was measured using D5 Series Automatic Driver G2 equipped with a D5 Calorimetry CoilSet device (nanoScale Biomagnetics SL) for water dispersions with a concentration equal to 10 mg/ml. In all measurements, dispersions were sonicated for 10 min just before measuring. Firstly, the role of the magnetite concentration on magnetic hyperthermia was determined for the water dispersions with concentrations equal to 3 mg/ml, 5 mg/ml, and 10 mg/ml. The measurements were performed for a constant frequency equal to 386.5 kHz and magnetic field strength of 27 kA/m. Next, the role of the frequency and magnetic field on the induced hyperthermia was studied for five sets of parameters: 304.7 kHz and 30 kA/m, 347.0 kHz and 26.3 kA/m, 386.5 kHz and 17.1 kA/m, 386.5 kHz and 23.65 kA/m and 386.5 kHz and 27 kA/m. All measurements were repeated three times for the freshly prepared dispersions. The reproducibility of the induced effect by the same dispersion (cyclic-induced hyperthermia) was tested for chosen sample by heating and cooling the same sample at 386.5 kHz and 27 kA/m five times. Finally, the magnetically induced hyperthermia was determined for much lower magnetic fields (5, 10, and 15 kA/m) and constant frequency (304.7 kHz).

**Cytotoxicity assay.** Human dermal fibroblasts (PDF1) were purchased from the American Type Cell Culture Collection (ATCC, Manassas, VA, USA). Cells were cultured in Dulbecco's Modified Eagles Medium (DMEM, Sigma Aldrich, Germany) with high glucose (5 g/L) and supplemented with 10% heat-inactivated Fetal Bovine Serum (FBS, PAN Biotech, Germany), antibiotics (1000 U/ml penicillin, 100 µg/ml streptomycin, 250 µg/ml amphotericin B (PAA Laboratories GmbH, Austria)) and 2 mM L-Glutamine (PAA Laboratories GmbH, Austria). To ensure the absence of the ethyl acetate, samples were washed with DI water and dried at 60 °C overnight. The stable nanoparticle dispersions with a starting concentration of 0.25 mg/ml in DI water were prepared for the experiments. Cells were cultured in a humidified atmosphere with 5% CO<sub>2</sub> at 37 °C. When obtaining 90% confluence cells were passaged to a new 75 cm<sup>2</sup> culture dish and reduced to 1:3. Cells at passage 9 were used for experiments. Cytotoxicity assays were performed in a 48-well plate format. A day before, test cells were seeded at a density of 25–10<sup>3</sup> cells per well in 250 µL of culture medium. The next day nanoparticles were added to reach a final concentration of 10, 25, 50, 75, and 100 µg/mL and incubated for 24, 48, and 72 h. After this time culture medium was replaced with 120 µL of 10% solution of AlamaBlue (Thermo Scientific, Germany) in the culture medium and incubated for 1 h. After this time, 100 µL were collected, and fluorescence was measured using VICTOR X5 multilabel plate reader (Perkin Elmer, USA) at EM/EX 590/560 nm. Results were presented as a percentage of control (untreated) cells. To visualize cells viability, after 72 h of incubation with nanoparticles, the culture medium was replaced with PBS containing 5 µg/ml of Ethidium Bromide (Thermo Scientific, Germany) and 0.2 nM of Fluorescein Diacetate (FDA, Sigma Aldrich, Germany), incubated for 10 min and observed under a fluorescent microscope.

**Ultrastructure of PDF1.** The ultrastructural changes in fibroblast cells were determined based on TEM analysis. Fibroblasts were treated with NPs at a 50 µg/ml concentration for 24, 48, and 72 h. Then detached by trypsinization, the cell suspension was prepared according to the standard TEM analysis method: washed, dehydrated, and embedded in epoxy resin (Epoxy Embedding Medium Kit; Sigma)<sup>39,40</sup>. Ultra-thin Sects. (70 nm) were cut on a Leica Ultracut UCT25 ultramicrotome and stained with uranyl acetate and lead citrate. The material was analyzed using a Hitachi H500 transmission electron microscope at 75 kV<sup>41</sup>.

## Results and discussion

**Magnetite nanoparticles' structure and morphology.** The structure and morphology of magnetite nanoparticles were studied using X-ray diffraction (XRD) and transmission electron microscopy (TEM). Firstly, the shape and size of magnetite nanoparticles were determined based on the TEM images analysis (Fig. 1a–h). As can be seen, in HAADF STEM (Fig. 1a–c) and TEM (Fig. 1d–f) images, all nanoparticles are characterized by nearly spherical shapes and form agglomerated structures in powder forms. Interestingly, only in the case of

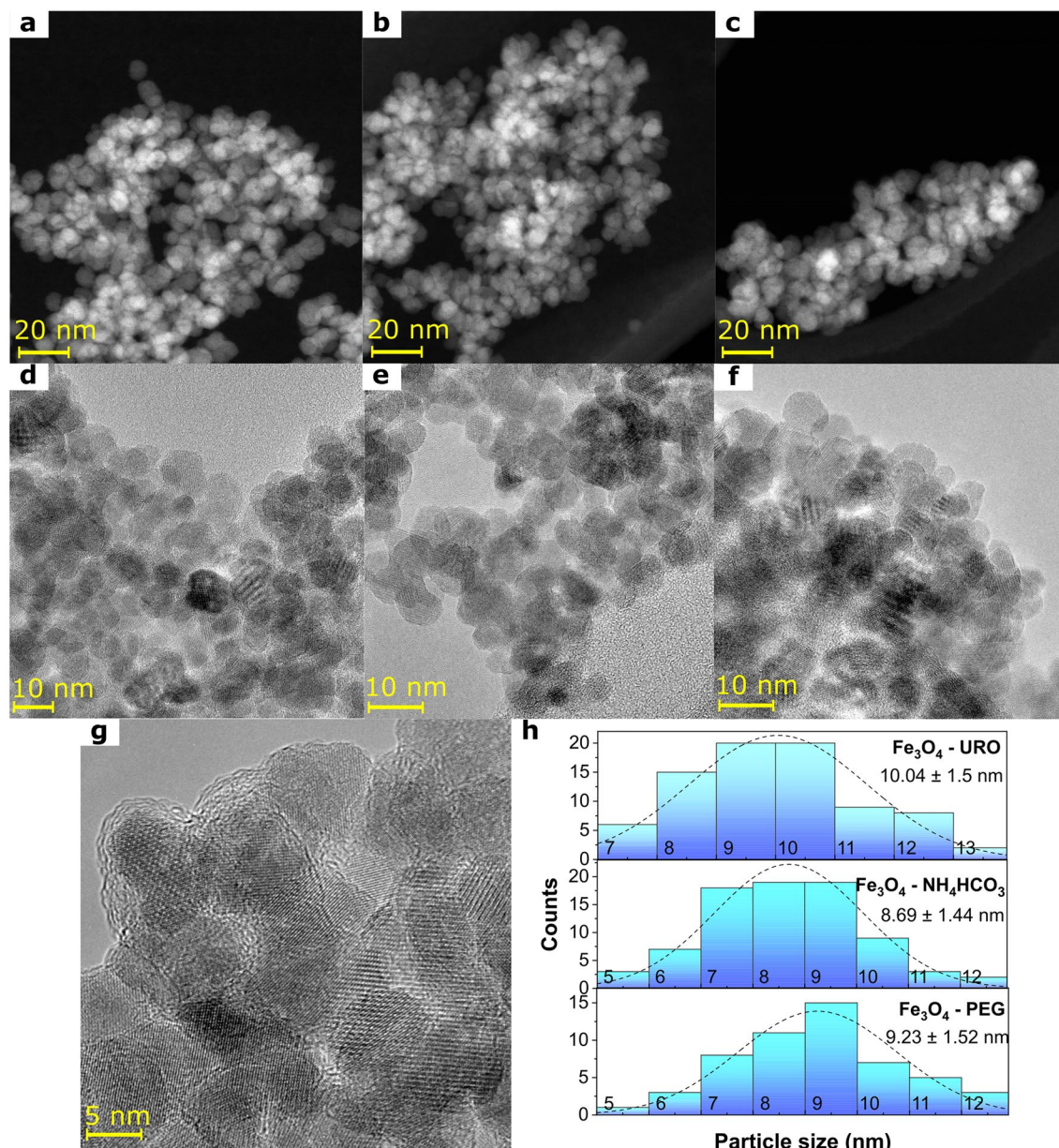


**Figure 1.** Results of transmission microscopy images analysis obtained for  $\text{Fe}_3\text{O}_4$ —URO NPs (**a, d**),  $\text{Fe}_3\text{O}_4$ — $\text{NH}_4\text{HCO}_3$  NPs (**b, e**) and  $\text{Fe}_3\text{O}_4$ —PEG NPs (**c, f**, and **g**); (**a–c**) high-angle annular dark-field scanning transmission electron microscopy images; (**d–g**) transmission electron microscopy images; (**h**) histograms of particle size distribution.

$\text{Fe}_3\text{O}_4$ —PEG NPs, the core–shell structure was observed in the TEM image (Fig. 1g), and this nanostructure is related to the visible, nanometric-size polymer coating. Moreover, it can be concluded that this amorphous-like shell is attributed to the presence of PEG on the magnetite core surface because this structure was not visible on TEM images for  $\text{Fe}_3\text{O}_4$ —URO and  $\text{Fe}_3\text{O}_4$ — $\text{NH}_4\text{HCO}_3$  NPs. The presence of a typical for magnetite spinel structure was confirmed based on the XRD patterns analysis (Fig. 2a). All identified diffraction peaks were attributed to the magnetite phase (Fd-3 m space group; 00-019-0629 card number). The observed broadening of the peaks is related mainly to nanosized materials' ultrafine crystallite size and internal strain. Accordingly, the average crystallite size ( $D_{XRD}$ ) was calculated using the Halder-Wagner method and is listed in Table 1. In this method influence of both ultrafine size and strain on the broadening of the diffraction peaks is considered according to the Eqs. (1)–(3)<sup>42–44</sup>.

$$\left(\frac{\beta^*}{d}\right)^2 = \frac{1}{D_{XRD}} \frac{\beta^*}{d^2} + \left(\frac{\varepsilon}{2}\right)^2 \quad (1)$$

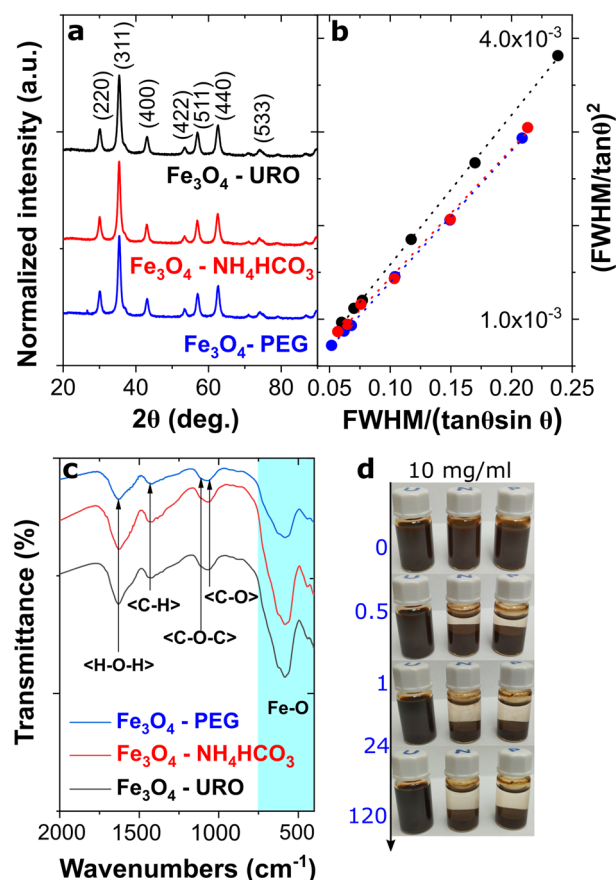


**Figure 2.** (a) XRD patterns of synthesized magnetite nanoparticles with characteristic Miller indices (Fd-3 m space group; 00-019-0629 card number), (b) Halder-Wagner plots from (220), (311), (400), (422), (440) and (511) diffraction peaks ( $R^2$  above 0.99 in all cases), (c) FTIR spectra of magnetite nanoparticles with marked identified vibrations related to the presence of the functionalized surface, (d) macroscopic images of the changes in the stability of colloidal dispersion of magnetite nanoparticles with high 10 mg/ml concentration in the time domain, i.e. from 0 to 120 h (from left:  $\text{Fe}_3\text{O}_4$ —URO NPs,  $\text{Fe}_3\text{O}_4$ — $\text{NH}_4\text{HCO}_3$  NPs and  $\text{Fe}_3\text{O}_4$ —PEG NPs).

Sample	$D_{\text{XRD}}$ (nm)	$D_{\text{TEM}}$ (nm)	$D_{\text{DLS}}$ (nm)	$\zeta$ potential (mV)
$\text{Fe}_3\text{O}_4$ —URO	9.06	$10.04 \pm 1.5$	$120.57 \pm 1.99$	$26.03 \pm 0.55$
$\text{Fe}_3\text{O}_4$ — $\text{NH}_4\text{HCO}_3$	10.51	$8.69 \pm 1.44$	$332.73 \pm 13.14$	$9.29 \pm 1.91$
$\text{Fe}_3\text{O}_4$ —PEG	10.31	$9.23 \pm 1.52$	$523.77 \pm 4.62$	$14.53 \pm 1.02$

**Table 1.** Comparison of the size of the nanoparticles determined based on the analysis of TEM images ( $D_{\text{TEM}}$ ) and average crystallite size calculated using the Halder-Wagner method ( $D_{\text{XRD}}$ ) together with the values of aggregates diameter measured using DLS technique ( $D_{\text{DLS}}$ ) and zeta potential values ( $\zeta$  potential) determined for the 10 mg/ml water dispersions.

$$\beta^* = \frac{(FWHM)\cos\theta}{\lambda} \quad (2)$$

$$d = \frac{2\sin\theta}{\lambda} \quad (3)$$

where  $D_{\text{XRD}}$  is the average crystallite size,  $\varepsilon$  is the microstrain,  $FWHM$  is the full width at half maximum of the diffraction peak,  $\theta$  is the diffraction angle, and  $\lambda$  is the X-ray wavelength. According to that, it is possible to rewrite Eq. (1) and determine  $D_{\text{XRD}}$  from the slope of the obtained curve on the Halder-Wagner plots (see Fig. 2b):

$$\left(\frac{FWHM}{\tan\theta}\right)^2 = \frac{K\lambda}{D_{\text{XRD}}}\frac{FWHM}{\tan\theta\sin\theta} + \left(\frac{\varepsilon}{2}\right)^2 \quad (4)$$

where  $K$  is a constant equal to 0.94 in the analyzed case of magnetite nanoparticles.

The influence of the synthesis method on the surface chemistry and colloidal stability in water was additionally tested, and obtained results are presented in Fig. 2c and d. As can be seen, despite using different modifiers, the magnetite surface in all cases was functionalized by the glycol molecules—triethylene for  $\text{Fe}_3\text{O}_4$ —URO NPs and  $\text{Fe}_3\text{O}_4$ — $\text{NH}_4\text{HCO}_3$  NPs and PEG on the surface of  $\text{Fe}_3\text{O}_4$ —PEG NPs, which is consistent with TEM images analysis. The absence of the N–H vibrations for samples synthesized using urotropine and  $\text{NH}_4\text{HCO}_3$  can be related to the decomposition of both compounds under the synthesis. Formed in this process products, including ammonia, can affect functionalization through interaction with the magnetite surface. However, the  $\text{NH}_4\text{HCO}_3$  decomposition appears at low temperatures, even below the temperature of  $\text{Fe}(\text{acac})_3$  decomposition; therefore, the role of this modifier should be much smaller than in the case of urotropine.

Typical for ultrafine magnetite nanoparticles, Fe–O bonds were observed in the range of 400–650  $\text{cm}^{-1}$ <sup>12</sup>. The C–O–C ether stretching vibration related to the presence of  $-\text{CH}_2-\text{OH}-\text{CH}_2-$  in glycols was observed at around 1100  $\text{cm}^{-1}$ <sup>45</sup>. Also, the characteristics of ethylene glycol-coated magnetite nanoparticle vibrations related to the C–H bending and C–O stretching were observed at around 1429 and 1054  $\text{cm}^{-1}$ , respectively<sup>35,46</sup>. Broad vibration at around 1633  $\text{cm}^{-1}$  corresponds to the H–O–H deformation peak<sup>47,48</sup>. Even though the glycol molecules functionalize all nanoparticles, and their size is similar, their colloidal stability is not the same. The most stable colloids were received from the  $\text{Fe}_3\text{O}_4$ —URO NPs, even at a high magnetite concentration of 10 mg/ml.  $\text{Fe}_3\text{O}_4$ — $\text{NH}_4\text{HCO}_3$  NPs and  $\text{Fe}_3\text{O}_4$ —PEG NPs sedimented in the dispersion quickly, after 30 min, while  $\text{Fe}_3\text{O}_4$ —URO NPs water dispersion without any sedimentation can be stored for five days and longer (Fig. 2d). According to the FTIR analysis, the urotropine does not functionalize the surface of  $\text{Fe}_3\text{O}_4$  but still plays a part in synthesizing nanoparticles with high colloidal stability. It is possible that the degradation products of the urotropine (i.e. ammonia and formaldehyde), which appear above 200 °C, play a part in this process<sup>49</sup>.

According to these unexpected observations, the zeta potential values ( $\zeta$  potential) and the aggregate diameter ( $D_{DLS}$ ) were measured using the dynamic light scattering (DLS) method for the water dispersions. The analysis results are presented in Table 1 for the dispersion with a concentration equal to 10 mg/ml. As can be seen, the magnetite nanoparticles synthesized in the presence of urotropine are characterized by the lowest aggregate diameter value, above 4-times lower than  $\text{Fe}_3\text{O}_4$ —PEG NPs and above 2.5-times lower than for  $\text{Fe}_3\text{O}_4$ — $\text{NH}_4\text{HCO}_3$  NPs. The same tendency was observed for the lower concentration value (Table S1); however, while the aggregate diameter value for  $\text{Fe}_3\text{O}_4$ —URO NPs do not depend on the dispersion concentration, the values of the  $D_{DLS}$  for two other samples are much lower compared to the 10 mg/ml dispersions. The  $\zeta$  potential of all nanoparticles is positive, characteristic of the coated magnetite nanoparticles<sup>35</sup>. Generally, nanoparticles with a zeta potential less than -25 mV and higher than +25 mV are characterized by high colloidal stability, which confirms the observations noted for the  $\text{Fe}_3\text{O}_4$ —URO dispersions. The  $\text{Fe}_3\text{O}_4$ — $\text{NH}_4\text{HCO}_3$  and  $\text{Fe}_3\text{O}_4$ —PEG have much lower  $\zeta$  potential values, equal to  $9.29 \pm 1.91$  and  $14.53 \pm 1.02$  mV, which result in the formation of much bigger aggregates and formation of unstable dispersions.

The zeta potential values differ for low (3 mg/ml; see Table S1) and high (10 mg/ml) concentrations. However, the similar  $\zeta$  potential changes between  $\text{Fe}_3\text{O}_4$ —URO,  $\text{Fe}_3\text{O}_4$ —PEG and  $\text{Fe}_3\text{O}_4$ — $\text{NH}_4\text{HCO}_3$  can be easily observed also for low concentration. These changes in zeta potential values are typical and discussed before by Kaszuba et al.<sup>50</sup>. According to their studies, obtained herein values (for high concentrations) must be treated as the relative zeta potential values, not absolute ones. However, it is more relevant than the absolute one because it describes the dispersions' properties, with a concentration equal to this one, which will be tested further in the magnetic hyperthermia measurements.

**Magnetic properties.** The nanoparticles, which can be used in magnetic hyperthermia applications, are mostly single-domain particles with superparamagnetic or ferromagnetic properties. Generally, the ferromagnetic properties, according to the larger hysteresis losses, generate more heat under alternating magnetic fields<sup>51</sup>. On the other hand, in the case of the superparamagnetic particles, while the external magnetic field is removed, the nanoparticles are completely unmagnetized, which results in their unique advantage for biomedical applications (not only as magnetic hyperthermia agents but also as drug delivery systems)<sup>52,53</sup>. Accordingly, the magnetic properties of synthesized nanoparticles were determined based on the VSM curves (Fig. 3). As can be seen, despite the different organic modifiers, all synthesized samples are characterized by a superparamagnetic state. Only slight differences between saturation magnetization ( $M_s$ ) can be observed. The highest value of  $M_s$  have  $\text{Fe}_3\text{O}_4$ —PEG and  $\text{Fe}_3\text{O}_4$ — $\text{NH}_4\text{HCO}_3$  NPs (60.4 and 60.1 emu/g), while  $\text{Fe}_3\text{O}_4$ —URO NPs have  $M_s$  equal to 57.5 emu/g. The changes in coercivity ( $H_c$ ) are also slight, and the value of this parameter is around 1 Oe, which confirms the superparamagnetic state of all magnetite nanoparticles.

**Magnetic hyperthermia.** Magnetic hyperthermia is one of the most promising cancer treatments, which is related to the possibility of using biocompatible magnetic nanoparticles such as magnetite and treatment of the cancer cells only locally without any significant negative impact on the healthy cells. Unfortunately, there is no one simple rule of the maximum temperature to which the tumour cells should be heated without impact on the healthy cells. Generally, this temperature should be in the range of 39–45 °C, above which thermal ablation of cells can occur<sup>24</sup>. In the case of the magnetic nanoparticles, the heat generated by them is related to Neel relaxation and Brownian relaxation. The first process relates to the reorientation of magnetic moments parallel to a magnetic field, while the second relates to the movement of whole nanoparticles in an external magnetic field<sup>54</sup>. Accordingly, the value of the generated thermal energy can be easily modified by synthesizing nanoparticles with different sizes, shapes, agglomeration ratios and even core–shell nanostructures and by the changes in alternating magnetic field (AMF) frequency and strength<sup>55</sup>.

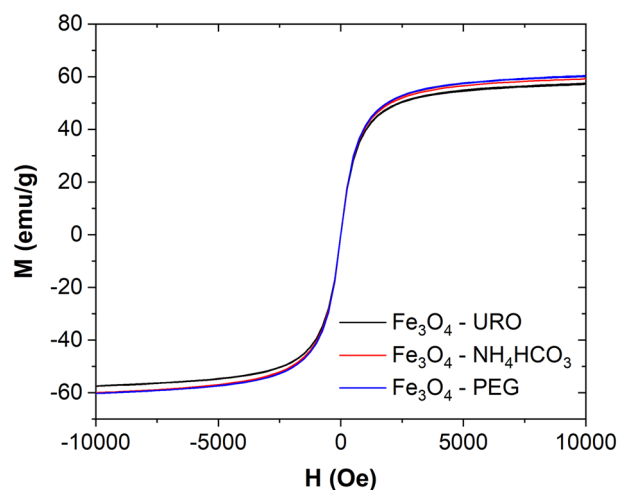


**Figure 3.** Hysteresis loops of the superparamagnetic magnetite nanoparticles synthesized in the presence of urotropine ( $\text{Fe}_3\text{O}_4$ —URO NPs),  $\text{NH}_4\text{HCO}_3$  ( $\text{Fe}_3\text{O}_4$ — $\text{NH}_4\text{HCO}_3$  NPs) and polyethylene glycol ( $\text{Fe}_3\text{O}_4$ —PEG NPs).

In the case of the magnetic-induced hyperthermia effect, various parameters influence the generated effect. Accordingly, this study determined the influence of magnetite nanoparticle concentration, AMF frequency ( $f$ ) and strength ( $H$ ) for  $\text{Fe}_3\text{O}_4$ —URO NPs,  $\text{Fe}_3\text{O}_4$ — $\text{NH}_4\text{HCO}_3$  NPs and  $\text{Fe}_3\text{O}_4$ —PEG NPs. Firstly, nanoparticle concentration influence on the magnetically induced hyperthermia was determined for three different concentrations, constant frequency, and magnetic field strength. Next, the influence of the frequency and strength was measured for high  $Hf$  parameters in the range of  $6.6 \cdot 10^9$  A/ms to  $10.4 \cdot 10^9$  A/ms following the newly developed application criteria, and the best sample was chosen to study specific absorption rate and intrinsic loss power parameters. The SAR (Specific Absorption Rate) determine the capacity of a magnetic material to absorb energy from an alternating magnetic field and is defined as the amount of power absorbed by the sample per mass unit. In the case of the studied magnetic colloids, this power can be expressed as the amount of energy converted into heat per time and mass. Accordingly, the SAR value can be calculated using Eq. (5).

$$\text{SAR} = \frac{1}{m_{np}} \frac{Q}{\Delta t} \quad (5)$$

where  $Q$  is the generated heat,  $m_{np}$  is the mass of the nanoparticles, and  $\Delta t$  is the time in which heat was generated. The generated heat in the used adiabatic system can be determined based on the calorimetric approach and expressed as:

$$Q = (m_{np}c_{np} + m_l c_l) \Delta T \quad (6)$$

where  $c_{np}$  and  $c_l$  are the specific heat capacity of the nanoparticles and liquid carrier and  $m_{np}$  and  $m_l$  mass of the nanoparticles and liquid carrier,  $\Delta T$  is the change in the temperature generated by the AMF. Assuming that the  $m_{np}c_{np} \ll m_l c_l$  and the colloid concentration of sample  $C$  is equal to  $m_{np}/V_l$  the SAR can be expressed as:

$$\text{SAR} = \frac{\delta_l c_l}{C} \left( \frac{\partial T}{\partial t} \right)_{max} \quad (7)$$

where  $\delta_l$  is the liquid carrier density, and  $\left( \frac{\partial T}{\partial t} \right)_{max}$  is the maximum heating rate of the colloid approximated by the modified Box-Lucas model (MBL):

$$\left( \frac{dT}{dt} \right)_{max} = A \cdot B = (T_{eq} - T_0) \frac{1}{\tau} \quad (8)$$

where  $T_{eq}$  is the equilibrium temperature of the colloid,  $T_0$  is the initial temperature of the colloid, and  $\tau$  is the characteristic heating time depending on sample properties. Accordingly, the SAR value can be expressed as:

$$\text{SAR} = \frac{\delta_l c_l}{C} (A \cdot B) \quad (9)$$

While the SAR depends on the magnetic field strength and frequency, the intrinsic loss power (ILP; Eq. 10) parameter was introduced to compare the laboratory results. However, the applicability of this parameter is also limited (dispersity of the sample must be higher than 0.1, the magnetic field must be below the saturation, the frequency must be in the range of  $10^5$  and  $10^9$  and also thermodynamic losses should be lower or equal to power

input)<sup>56</sup>. Furthermore, this parameter assumes the quadratic dependence with the magnetic field ( $H$ ) and linear dependency with frequency ( $f$ ) of the SAR parameter and is correct, while linear response theory can be applied<sup>57</sup>.

$$ILP = \frac{SAR}{fH^2} \quad (10)$$

Various models were proposed in the literature to describe magnetically induced hyperthermia, including linear response theory (LRT), Stoner–Wohlfarth model and equilibrium functions<sup>58</sup>. For the superparamagnetic nanoparticles approximation of heat generated by them was proposed as LRT by Rosensweig<sup>59</sup>, in which dissipated power ( $P$ ) can be represented as:

$$P = \pi \mu_0 \chi'' H^2 f \quad (11)$$

where  $\mu_0$  is the permeability of free space,  $\chi''$  is the imaginary part of complex susceptibility,  $H$  is the magnetic field strength, and  $f$  is the magnetic field frequency. Various factors restrict the applicability of this model, while the most important one is small magnetic fields, for which the assumption is that the magnetization changes linearly with increasing the magnetic field can be applied<sup>60</sup>. Accordingly, the possible applicability of LRT in the studied magnetite nanoparticles was first verified. As can be seen in Fig. S1, two regions can be observed. While the magnetic field is equal to or lower than 17.1 kA/m, the LRT can be applied to describe the behaviour of synthesized superparamagnetic nanoparticles. Above that field value, this model cannot be applied, which is consistent with the literature data<sup>60</sup>. This LRT region obeys results obtained for all synthesized samples and  $H \cdot f$  product from  $1.52$  to  $6.61 \cdot 10^9$  A/ms. Therefore obtained ILP values (calculated only for this region) can be compared with other literature data, for which LRT also can be successfully applied to describe magnetically induced hyperthermia.

The influence of the magnetite nanoparticle concentration on the SAR value is nonlinear<sup>61,62</sup>. Accordingly, three concentrations were measured to determine the optimum concentration for further characterization. The typical non-monotonic behaviour was observed (see Fig. S2). While the highest SAR values were observed for the 10 mg/ml concentration, the lowest SAR values were obtained for all 5 mg/ml magnetite nanoparticles colloids, despite the differences between their colloidal stability and aggregate size. The presented behaviour is typical for the transition between the single-particle scenario (observed for 3 mg/ml dispersions) and the collective-particle scenario observed and described by Conde-Leboran et al.<sup>61,62</sup>.

According to the above, the 10 mg/ml concentration was chosen for further analysis, for which a relatively high magnetically induced hyperthermia effect is related to the formation of collective particles. The frequency and magnetic field strength analysis on the SAR and ILP parameters are presented in Fig. 4 and Table 2. As can be seen, the temperature changes generated by the external AMF are different for all samples. Only  $\text{Fe}_3\text{O}_4$ — $\text{NH}_4\text{HCO}_3$  NPs are characterized by ultrafast temperature growth in all tested frequencies and magnetic field strength. This can be related to the relatively high aggregate diameter ( $332.73 \pm 13.14$  nm) and lowest zeta potential value equal to  $9.29 \pm 1.91$  mV, which reflects the higher tendency to form aggregates. For other samples, a slow temperature increase can be observed, especially using 386.5 kHz and 17.1 kA/m. What is essential, for the  $\text{Fe}_3\text{O}_4$ — $\text{NH}_4\text{HCO}_3$  NPs also, the highest SAR ( $69.6 \pm 5.2$  W/g) and ILP ( $0.613 \pm 0.051$  nHm<sup>2</sup>/kg) values observed for the lowest tested  $H \cdot f$  parameter equal to only  $6.6 \cdot 10^9$  A/ms, while for example, for the  $\text{Fe}_3\text{O}_4$ —URO NPs the highest SAR was equal only to  $38.8 \pm 1.3$  W/g for the  $H \cdot f$  equal to  $10.4 \cdot 10^9$  A/ms. Moreover, calculated SAR and ILP values are the highest for nanoparticles synthesized in the presence of  $\text{NH}_4\text{HCO}_3$  in all analyzed frequency and magnetic field ranges. This phenomenon can be related to collective behavior (aggregation of ultrafine nanoparticles). However, the changes between magnetic hyperthermia behavior and aggregate size are complex, and various (sometimes opposites) models were proposed<sup>63</sup>.

Moreover, the changes in aggregate size and even shape (formation of the chains under applied magnetic field) also affect the SAR value<sup>13</sup>. The theoretical modeling performed by Abu-Bakr et al.<sup>64</sup> shows that the clusterization of nanoparticles decreases the thermal effect. Similar findings were presented in<sup>65</sup> and can be used to describe changes between SAR values of  $\text{Fe}_3\text{O}_4$ — $\text{NH}_4\text{HCO}_3$  NPs and  $\text{Fe}_3\text{O}_4$ —PEG NPs (nanoparticles synthesized in presence of PEG have a higher aggregate diameter, therefore, have lower SAR values in the analyzed frequency and field strength range). In the case of the sample synthesized in the presence of urotropine, it is expected that according to the high colloidal stability and the smallest aggregate size, it should have the highest SAR values, which were not observed herein. This behavior can be related to the changes in the magnetic behavior of the ferrofluid. As mentioned previously, an analyzed concentration equal to 10 mg/ml resulted in appearing of a collective-particle scenario. Therefore, observed changes in SAR values are related to the heat generated not by a single superparamagnetic nanoparticle but by aggregates. Although, as seen in Fig. S2, the changes generated by the aggregate size are not linear, the size of  $\text{Fe}_3\text{O}_4$ — $\text{NH}_4\text{HCO}_3$  NPs aggregates is probably optimal, in which magnetic hyperthermia effect in the collective-particle scenario is the highest. The mechanism responsible for that is still unknown; however, it can be related to the evolution of aggregate size and shape under measurement<sup>13</sup>.

The reproducibility of the same magnetofluid in the case of cyclic magnetically induced hyperthermia was checked and presented in Fig. 5. As can be seen, the sample characterized by the highest SAR value ( $\text{Fe}_3\text{O}_4$ — $\text{NH}_4\text{HCO}_3$  NPs) cannot be used for cyclic magnetically induced hyperthermia; the SAR decreases from 93.17 W/g to 57.06 W/g. Interestingly, the highest decreases were observed in the two first runs ( $\Delta$  SAR equal to 17.29 W/g); afterwards, SAR stabilized at about 60 W/g. Moreover, the changes induced by the magnetic field change from exponential to linear behaviour. Interestingly, in the case of the  $\text{Fe}_3\text{O}_4$ —PEG NPs, the changes are not so visible, and SAR remain at a similar level (for example, 48.97 W/g for the first and 47.04 for the fourth run); also, temperature changes has typical exponential behaviour in the whole experiment. The lowest changes were observed for the  $\text{Fe}_3\text{O}_4$ —URO NPs, for which SAR remained at the same level throughout the experiment. i.e.



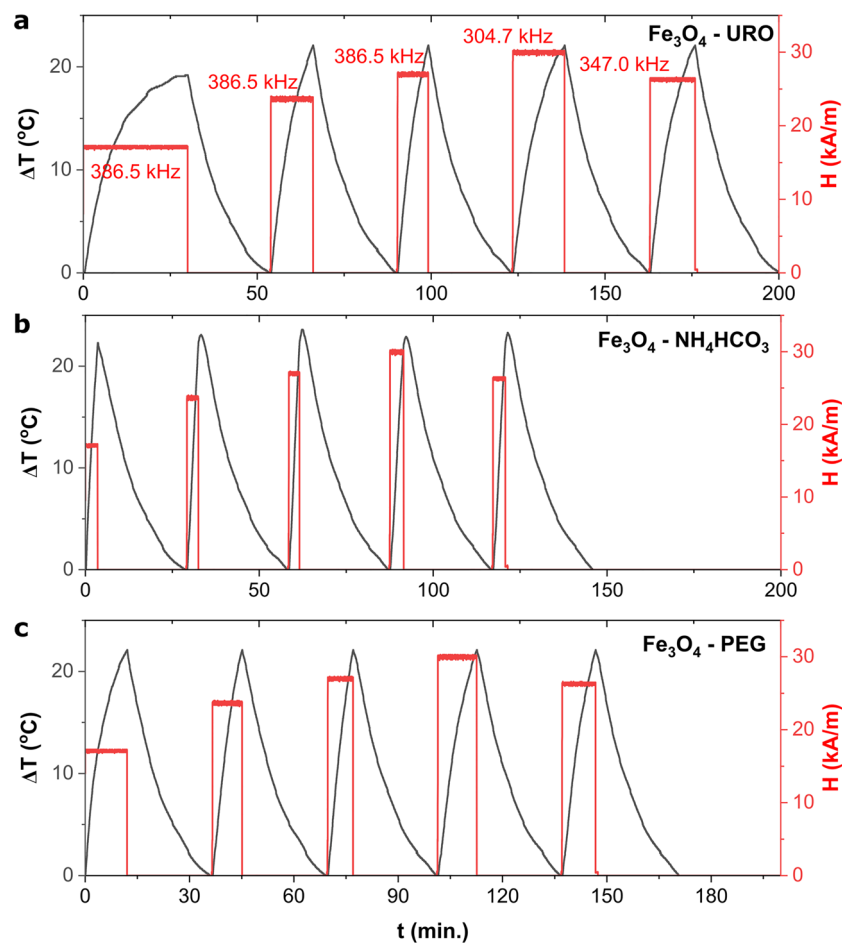


**Figure 4.** Influence of magnetic field (frequency and strength) on the temperature changes induced by magnetite nanoparticles dispersions with a concentration of 10 mg/ml measured for  $\text{Fe}_3\text{O}_4$ —URO NPs (a),  $\text{Fe}_3\text{O}_4$ — $\text{NH}_4\text{HCO}_3$  NPs (b) and  $\text{Fe}_3\text{O}_4$ —PEG NPs (c).

Frequency (kHz)	Field intensity (kA/m)	SAR (W/g)	ILP (nHm <sup>2</sup> /kg)
<b><math>\text{Fe}_3\text{O}_4</math>—URO NPs</b>			
386.5	17.1	13.4 ± 2.0	0.119 ± 0.018
386.5	23.65	31.8 ± 0.5	n.a
386.5	27	38.8 ± 1.3	n.a
304.7	30	28.2 ± 1.5	n.a
347.0	26.3	30.2 ± 2.2	n.a
<b><math>\text{Fe}_3\text{O}_4</math>—<math>\text{NH}_4\text{HCO}_3</math> NPs</b>			
386.5	17.1	69.6 ± 5.2	0.613 ± 0.051
386.5	23.65	48.4 ± 3.0	n.a
386.5	27	52.7 ± 2.9	n.a
304.7	30	42.6 ± 3.7	n.a
347.0	26.3	45.1 ± 1.9	n.a
<b><math>\text{Fe}_3\text{O}_4</math>—PEG NPs</b>			
386.5	17.1	25.8 ± 2.8	0.228 ± 0.025
386.5	23.65	36.8 ± 1.7	n.a
386.5	27	42.7 ± 2.9	n.a
304.7	30	35.0 ± 1.7	n.a
347.0	26.3	38.4 ± 0.2	n.a

**Table 2.** Specific absorption rate (SAR) and intrinsic loss power (ILP) calculated for magnetite nanoparticles dispersions (10 mg/ml).

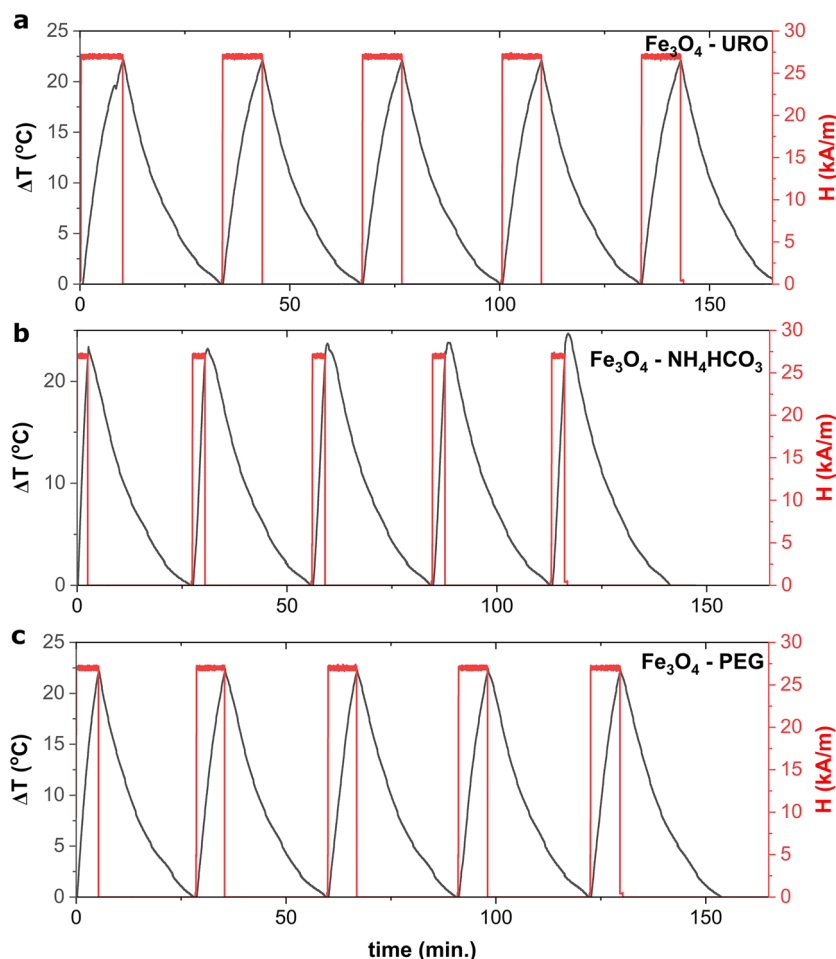


**Figure 5.** Repeatability of hyperthermia induced by the same sample of magnetite nanoparticles with the concentration of 10 mg/ml and in the constant alternative magnetic field parameters (386.5 kHz, 27 kA/m).

average SAR is equal to  $33.20 \pm 1.15$  W/g. It can be noted that when  $\zeta$  potential decreases from  $26.03 \pm 0.55$  to  $9.29 \pm 1.91$  mV, the SAR stability also decreases. This behavior can be related to the agglomeration of nanoparticles under external magnetic fields. After the stable agglomerates' formation, the SAR value remains similar.

If we look at the potential application of this cyclic-induced hyperthermia effect, one of the most important use is controlled drug release therapy. For example, magnetite nanoparticles can be coated by thermoresponsive polymers to ensure that the drug is released only when the temperature rises. Ferjaoui et al.<sup>4</sup> have shown that the synthesis of the core/shell magnetite-based nanoparticles with doxorubicin-loaded thermoresponsive copolymer shell composed of 2-(2-methoxy)ethyl methacrylate and oligo(ethylene glycol)methacrylate results in the formation of the nanostructure, in which drug release with higher yield can be observed when the temperature raises. The possibility of the controlled release of small doses of anticancer drugs supported by the magnetically induced hyperthermia for a long time only close to the cancer cells should be another approach to decrease the toxicity of the anticancer drugs on healthy cells. Accordingly, stable and repeatable heating properties should be required; therefore,  $\text{Fe}_3\text{O}_4$ —URO NPs with the lowest  $\Delta\text{SAR}$  value would be a better choice than  $\text{Fe}_3\text{O}_4$ — $\text{NH}_4\text{HCO}_3$  NPs characterized by the highest SAR values.

One of the most critical parameters influencing magnetic hyperthermia is magnetic field frequency and strength. The first commercially developed equipment to treat human patients works at a frequency of 100 kHz with a magnetic field strength equal to 18 kA/m<sup>66</sup>. In the case of the frequency choice, many studies mentioned which is safe for the body ranges. For example, Khan et al. proposed clinical trials ranging from 50 kHz to 2 MHz to avoid skeletal muscle stimulations and magnetic field penetration to the depth tissue<sup>67</sup>. Other research limited the frequency range to 0.1 MHz, above which the peripheral nerve excitation threshold can be significantly raised. To choose the magnetic field strength, the Atkinson-Brezovich criterion or modified version proposed by Hergt and Dutz should be applied<sup>68,69</sup>. According to the modified version, the product between frequency and magnetic field strength should be lower than  $5 \cdot 10^9$  A/ms when the magnetic hyperthermia is limited to the small body part. However, while the Atkinson-Brezovich criterion was introduced based on the testing of the discomfort of the person treated using a loop with a diameter of about 30 cm, the others were not experimentally tested, especially on the functions of cells<sup>60</sup>. Considering that the novel magnetically induced hyperthermia is based on nanoparticles, not micro-sized implants, these criteria should be revised one more time. For example,

Bellizzi et al.<sup>70,71</sup> showed that the new criterion could be even two orders of magnitude larger than proposed by Atkinson-Brezovich. Moreover, there are various ways to extend this limit and factors which influence the negative impact of AMF on healthy tissue, such as coil type or use of intermittent AMF<sup>72</sup>.

Accordingly, the influence of the magnetic field on the hyperthermia effect was measured for a fixed frequency equal to 304.7 kHz and three various magnetic fields to comply with the mentioned application criteria. The analysis results are presented in Fig. 6. As can be seen, the differences between tested nanoparticles are visible in the case of both ILP and SAR analysis. The highest SAR and ILP values were received for nanoparticles synthesized in the presence of  $\text{NH}_4\text{HCO}_3$ , while the lowest ones characterized  $\text{Fe}_3\text{O}_4$ -URO. While the  $Hf$  product increases from  $1.52 \cdot 10^9$  A/ms to  $4.57 \cdot 10^9$  A/ms, the SAR value increases in all cases; however, the same tendency for ILP was observed only for  $\text{Fe}_3\text{O}_4$ -URO. In the case of  $\text{Fe}_3\text{O}_4$ - $\text{NH}_4\text{HCO}_3$  and  $\text{Fe}_3\text{O}_4$ -PEG NPS with increasing  $Hf$  product, the ILP decreases. Therefore, despite the high dispersion stability, the  $\text{Fe}_3\text{O}_4$ -URO NPs are characterized by ultralow magnetically induced hyperthermia effect and can be used with higher  $Hf$  values or for other applications such as drug delivery systems or multifunctional platforms, which dose drugs from the thermoresponsive polymers. In applying nanoparticles for the pure magnetically induced hyperthermia, the  $\text{Fe}_3\text{O}_4$ - $\text{NH}_4\text{HCO}_3$  should be chosen according to the high SAR and ILP values for all  $Hf$  products (also, higher ones discussed previously in this work).

The applicability of magnetite and ferrites nanoparticles in magnetically induced hyperthermia treatment is widely studied. For similar  $Hf$  values, it can be seen that higher SAR values have the  $\text{Fe}_3\text{O}_4$ - $\text{NH}_4\text{HCO}_3$  NPs than, for example, tetragonal  $\text{Mg}_{0.1}\text{Zn}_{0.7}\text{Co}_{0.2}\text{Fe}_2\text{O}_4$  and  $\text{Mg}_{0.15}\text{Zn}_{0.65}\text{Co}_{0.2}\text{Fe}_2\text{O}_4$  NPs, for which SAR was around 3.5 and 7.0 W/g for  $3.2 \cdot 10^9$  A/ms. However, obtained results are nearly two times lower than for  $\text{Mg}_{0.5}\text{Zn}_{0.3}\text{Co}_{0.2}\text{Fe}_2\text{O}_4$  NPs, for which SAR was equal to 82.7 W/g<sup>73</sup>. A more interesting comparison can be made based on the data reported by Kullumadil et al.<sup>57</sup>, which introduced the ILP parameter and calculated its value for various commercially available colloids dedicated to magnetic hyperthermia. The tested by them colloids had higher concentrations even above 50 mg/ml; however, obtained herein ILP values for low H-region, in which LRT can be applied, are still higher than, for example, commercially available BNF-02008, BNF-01708, and BNF-01808 (Micromod) with a concentration of 50, 80 and 90 mg/ml, respectively (for both  $\text{Fe}_3\text{O}_4$ -PEG<sub>3</sub> NPs and  $\text{Fe}_3\text{O}_4$ - $\text{NH}_4\text{HCO}_3$  NPs). For the  $\text{Fe}_3\text{O}_4$ - $\text{NH}_4\text{HCO}_3$  NPs, SAR and ILP values were much higher for lower  $Hf$  product (equal to  $1.52 \cdot 10^9$  A/ms) and equal to  $11.8 \pm 2.2$  W/g and  $1.496 \pm 0.314$  nHm<sup>2</sup>/kg.

**Magnetite nanoparticles cytotoxicity.** Human fibroblasts are used as model cells to study various biological processes because they are involved in the regeneration of tissue damage. Therefore, they can be used as an indicator of the cytotoxicity of nanoparticles used in medicine<sup>74,75</sup>. The first toxicity assay, performed after 24 h of cells incubation with nanoparticles, showed only a slight decrease in cells viability in all tested NPs concentrations (Fig. 7). No differences were observed between the NPs modification. Microscopy analysis of the cell culture revealed that all introduced NPs precipitated from the culture medium and settled down on the cell layer (Fig. S3). Similar data were obtained after 48 h of incubation with NPs, where cells viability decreased only slightly. A more significant decrease in AlamarBlue reduction was detected after 72 h incubation with NPs. The decrease was dose-dependent and most significant at the highest tested concentration of NPs, but cells viability did not drop below 50% of control-untreated cells (Fig. 7). There are no differences in toxicity between types of  $\text{Fe}_3\text{O}_4$  NPs tested for toxicity to dermal fibroblasts at any time. To visualize cells viability by fluorescent microscopy, staining with Ethidium bromide (dead cells—red fluorescence) and Fluorescein Diacetate (live cells—green fluorescence) were performed at 72 h. All treated cells appeared as viable (green fluorescence) (Fig. 8).

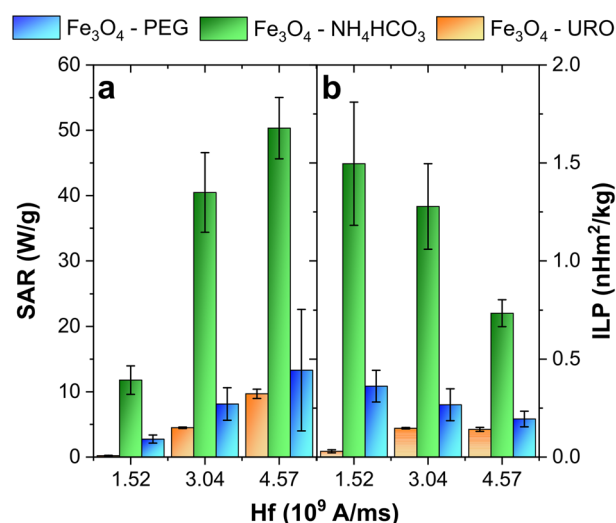


**Figure 6.** Influence of the  $Hf$  value on the SAR and ILP parameters determined for  $\text{Fe}_3\text{O}_4$ -URO,  $\text{Fe}_3\text{O}_4$ - $\text{NH}_4\text{HCO}_3$  and  $\text{Fe}_3\text{O}_4$ -PEG NPs water dispersion with a concentration of 10 mg/ml (for constant field frequency equal to 304.7 kHz).

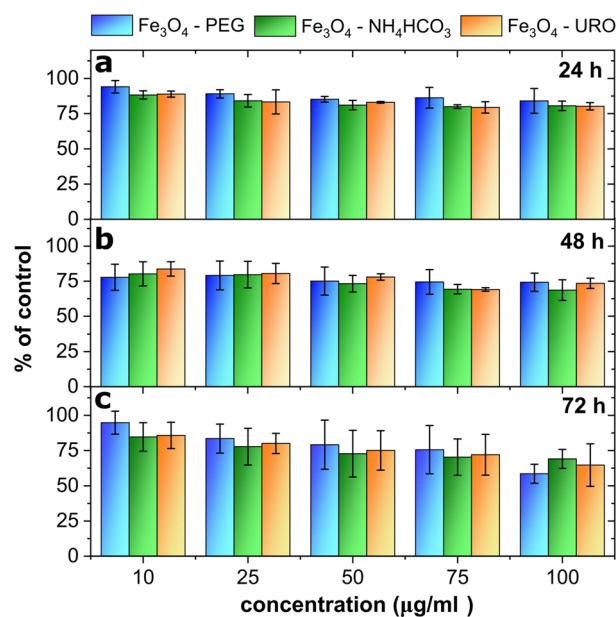


**Figure 7.** Cytotoxicity of nanoparticles (Fe<sub>3</sub>O<sub>4</sub>—URO NPs, Fe<sub>3</sub>O<sub>4</sub>—NH<sub>4</sub>HCO<sub>3</sub> NPs and Fe<sub>3</sub>O<sub>4</sub>—PEG NPs) to dermal fibroblasts determined after (a) 24 h, (b) 48 h and (c) 72 h for wide concentration range from 10 to 100 µg/ml.

Ultrastructural analysis of NP-treated cells was performed to test whether NPs entered into the cells. Control, untreated cells (marked as 0 group), at each time point (24, 48, and 72 h of the experiment) remained unchanged. The ultrastructure of these cells was taken as the reference for each experimental group at indicated time points (Fig. 9A, B). Numerous flocculent-granular patches of electron-dense material (magnetite nanoparticles) were detected in all experimental groups and time points (Figs. 9C–H, S4C–H, and S5C–H). The material accumulated in the membranous vesicles resembled autophagosomes (Fig. 9C, D, G, H). This material was also observed near the outer surface of the fibroblasts, adhering to their cell membrane. These granules were surrounded by fibroblast cytoplasmic projections and entered their cytoplasm by phagocytosis. The amount of electron-dense material was proportional to the incubation time. Analysis of the cytoplasmic structures of the treated cells in all experimental groups revealed a gradual increase in the number of autophagous structures (autophagosomes, autolysosomes, and residual bodies). Apart from the autophagous structures mentioned, there were no other significant changes in the ultrastructure of treated cells.

Tested nanoparticle seems to be non-toxic to cells *in vitro* with a shorter incubation time, and only a little toxic effect appears at high doses of NPs after 72 h (Fig. 7), but since all tested Fe<sub>3</sub>O<sub>4</sub> NPs precipitated (Fig. S3), these results require depth discussion. When NPs settled down, the local concentration of NPs at the bottom of the culture dish increased, and the cells there experienced a much higher concentration of NPs, as assumed in the experiment, suggesting even lower toxicity of tested NPs. On the other hand, NPs precipitation can limit their interaction with cells. We do not know whether precipitation is due to NPs aggregation and precipitation or interaction with cell culture medium compounds. The culture medium contains many organic and inorganic compounds such as ions, glucose, aminoacids, and proteins. It is known that ion presence can affect the NP aggregation<sup>76</sup>. Also, serum proteins in the culture medium, especially albumins, can interact with NPs creating protein corona around NPs. The presence of protein corona has a rather positive effect, as it prevents NPs from direct interaction with cell membrane decreasing their toxicity<sup>77</sup>. As all tested Fe<sub>3</sub>O<sub>4</sub> NPs precipitated, any introduced surface modification did not prevent them from interacting with culture medium compounds. As precipitation limits the interaction of NPs with cells and may be the reason for low toxicity, we can indeed conclude from ultrastructural analysis that NPs interact with the cell surface and enter cells by endocytosis. This can suggest that despite NPs precipitation, cells experience NPs effect, which may confirm the reliability of the results. Since these tests were performed *in vitro*, and many compounds present in the culture medium are also found in body fluids such as blood or lymph, we can predict that *in vivo* toxicity of Fe<sub>3</sub>O<sub>4</sub> NPs appears to be low, but further studies should verify this.

Interaction of NPs with the cell membrane can lead to its destruction and cause rapid, necrotic cell death. As revealed by ultrastructural analysis, NPs are in contact with cells' surfaces. The observed toxicity appeared slowly, and we did not observe an accumulation of dead cells in the treated culture; thus, necrosis was excluded. The primary mechanism of toxicity reduction by PEG coating is preventing plasma membrane disruption<sup>28</sup>; thus, the low toxicity of Fe<sub>3</sub>O<sub>4</sub>—PEG NPs may be due to the presence of nanometric polymer coating (see Fig. 1g). As all modified NPs have the same toxicity level, this suggests that NH<sub>4</sub>HCO<sub>3</sub> and URO modification work as good as PEG in toxicity reduction.

Because toxicity appears only after a longer incubation time at high doses of NPs, it can result from damage accumulation caused by NPs inside the cells. Iron nanoparticles, in proper condition, can cause a certain type

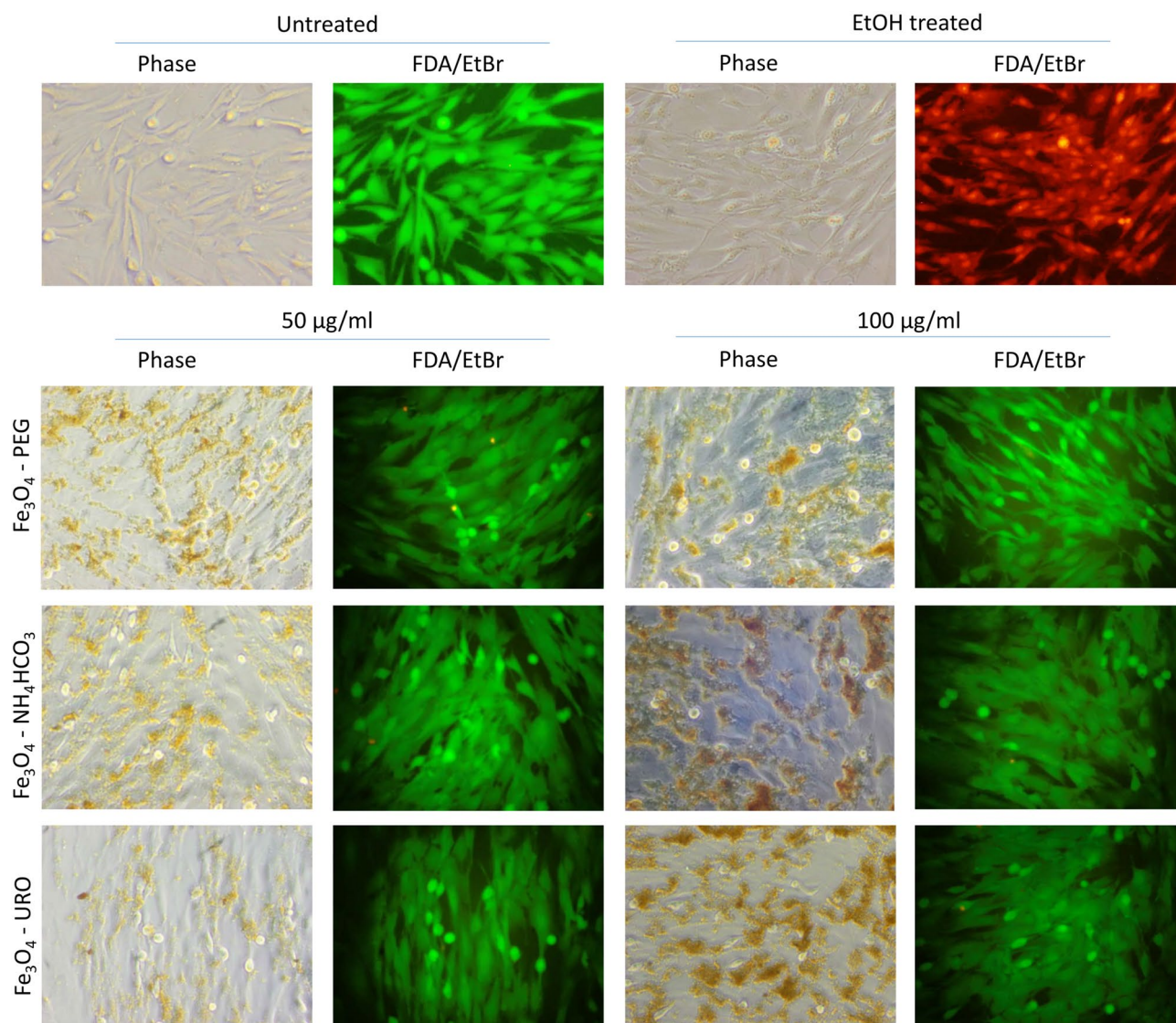


**Figure 8.** The viability of cells treated with nanoparticles visualized by FDA/EtBr staining after 72 h of culture in the presence of NPs. Cells treated with nanoparticles appear to be alive (green fluorescence). Cells treated with 70% EtOH as a positive control for dead cells characterized by red fluorescence.

of programmed cell death called ferroptosis<sup>78</sup>. Since FDA/EtBr dual staining showed no increase in the number of dead cells (Fig. 8), the decrease in AlamarBlue reduction has other reasons than cell death. Ultrastructural analysis revealed strong induction of the autophagic process in treated cells (Figs. 9, S4, and S5). Autophagy is a physiological process where damaged organelles are degraded, enabling cell regeneration. An increase in the autophagy process is observed in response to hunger or stress.

Induction of autophagy in cells is reported for many types of NPs. It is postulated that autophagy plays a dual role in NPs toxicity. Negative, causing toxicity as intense autophagy can lead to autophagic cell death and protection by sequestering NPs in autophagosomes and preventing them from interacting with other organelles inside the cell<sup>79,80</sup>. Nevertheless, the autophagic process alters the metabolic process in cells<sup>81</sup>. Thus, decreased alamar reduction may result from intensive autophagy in NPs treated cells. Intensive autophagy inhibits cell growth and proliferation; therefore, lower resazurin reduction can be an effect of decreased cell proliferation. This is more likely as the difference in cells proliferation needs more time to be visible in the metabolic assay. Since the exact mechanism of autophagy induction by NPs remains unknown, it has been noted that Fe<sub>3</sub>O<sub>4</sub> NPs increase the production of reactive oxygen species (ROS) in dermal fibroblasts and cause oxidative stress<sup>82</sup>. Damage caused by ROS in cellular structures can induce autophagy<sup>75</sup>. We have not tested oxidative stress markers in Fe<sub>3</sub>O<sub>4</sub> NPs treated cells, but induction of autophagy is certainly a cell response to the presence of NP in the culture medium; therefore, the overall role of autophagy induction in NP toxicity should be investigated.

As stated before, toxicity seems to affect internal cellular stress. Since NPs enter cells through endocytosis, various biological processes and enzymes can alter their chemical and physiological properties, making them more toxic upon entry into cells. It is unknown to what extent the modifications introduced are stable in biological structures, but the fact that cells react to all tested NPs, in the same way, suggests that autophagy relies solely

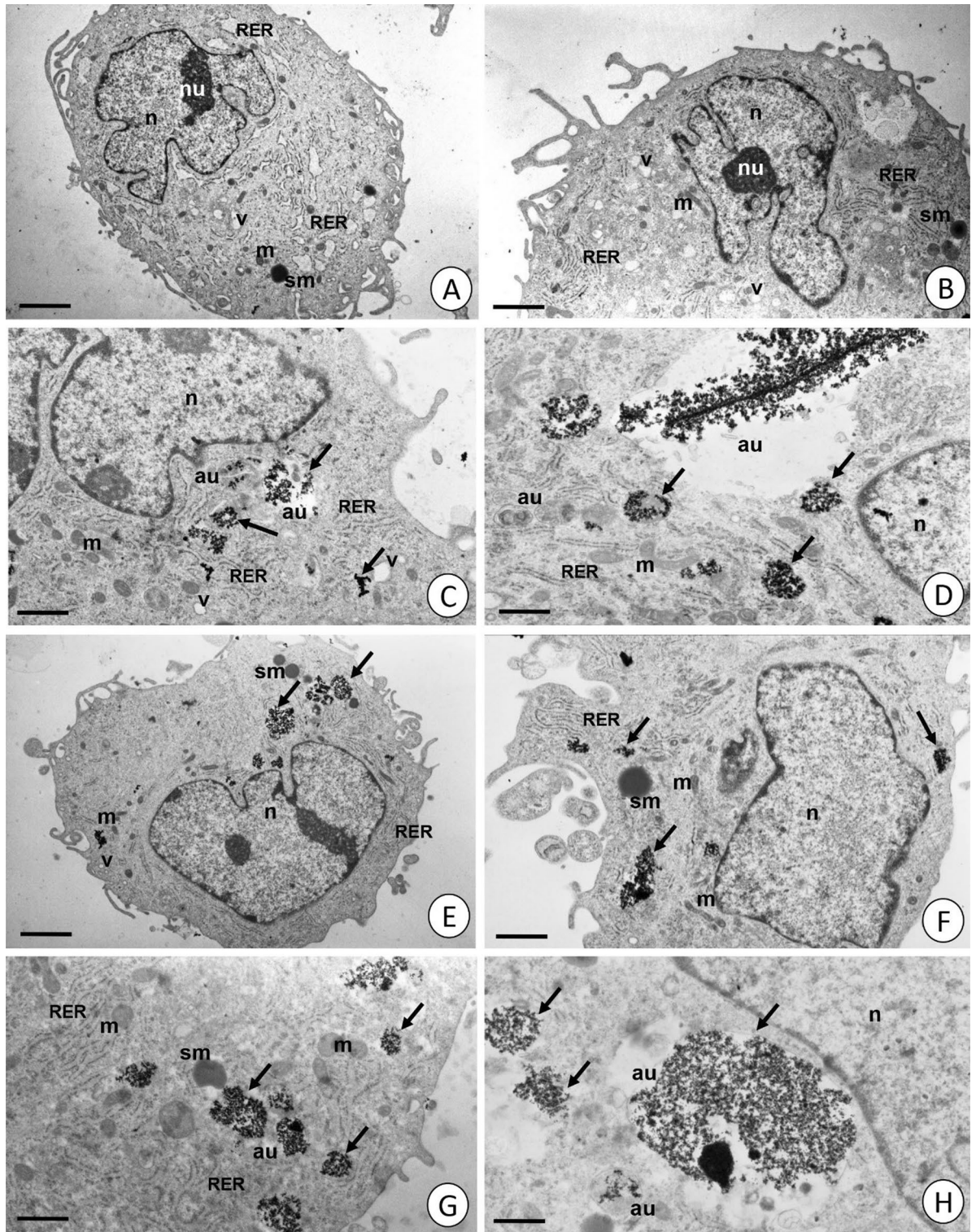


**Figure 9.** Fibroblasts visible in TEM. (A, B) 0 – 72 h control group. (C, D)  $\text{Fe}_3\text{O}_4$ –PEG – 72 h experimental group. (E, F)  $\text{Fe}_3\text{O}_4$ – $\text{NH}_4\text{HCO}_3$  – 72 h experimental group. (G, H)  $\text{Fe}_3\text{O}_4$ –URO – 72 h experimental group. Nuclei (n), mitochondria (m), cisterns of RER (RER), storage material (sm), vacuoles (v), autophagosomes (au), electron-dense granules (arrows). (A) Scale bar = 2,37  $\mu\text{m}$ . (B) Scale bar = 1,60  $\mu\text{m}$ . (C) Scale bar = 1,05  $\mu\text{m}$ . (D) Scale bar = 0,73  $\mu\text{m}$ . (E) Scale bar = 1,16  $\mu\text{m}$ . (F) Scale bar = 1,18  $\mu\text{m}$ . (G) Scale bar = 0,92  $\mu\text{m}$ . (H) Scale bar = 0,81  $\mu\text{m}$ .

on the NP's core. Further research requires studying magnetite nanoparticles' physical and chemical changes inside cells to confirm this.

## Conclusions

Ultrafine, superparamagnetic spherical magnetite nanoparticles functionalized by triethylene glycol or polyethylene glycol were successfully synthesized using the polyol method. It was confirmed that using urotropine significantly improves the colloidal stability of the water dispersions, even at a high concentration level of 10 mg/ml. While the differences in the size of the nanoparticles are negligible ( $8.69 \pm 1.44$  nm for the smallest  $\text{Fe}_3\text{O}_4\text{—NH}_4\text{HCO}_3$  and  $10.04 \pm 1.5$  nm for the biggest  $\text{Fe}_3\text{O}_4\text{—URO}$  NPs), the magnetically induced hyperthermia effect is dependent on the type of used nanoparticles. This behavior is related to the differences in the aggregate size and zeta potential values. Only  $\text{Fe}_3\text{O}_4\text{—NH}_4\text{HCO}_3$  NPs are characterized by ultrafast temperature growth in all tested frequencies and magnetic field strength, which is highly visible for low  $H \cdot f$  product values. For  $6.6 \cdot 10^9$  A/ms, these nanoparticles had the highest SAR ( $69.6 \pm 5.2$  W/g) value, while  $\text{Fe}_3\text{O}_4\text{—URO}$  NPs with the highest colloidal stability had SAR equal to  $13.4 \pm 2.0$  W/g. Unfortunately, these nanoparticles synthesized in the presence of  $\text{NH}_4\text{HCO}_3$  cannot be used for cyclic-induced hyperthermia according to the losses in efficiency. These losses were not observed for  $\text{Fe}_3\text{O}_4\text{—URO}$  NPs, for which the average SAR was equal to  $33.20 \pm 1.15$  W/g.

Moreover, LRT can be applied for low H-field region (up to 17.1 kA/m). Based on this finding, synthesized herein nanoparticles are characterized by higher ILP values than some commercially available dispersions with much higher (even 8 times) concentrations. The cytotoxicity tests show no differences between toxicity on human fibroblasts for all three nanoparticle types, and the highest toxicity was observed for high nanoparticle concentrations and high interaction times with fibroblast cells. Also, ultrastructural analysis confirmed that the nanoparticles do not significantly affect the fibroblasts, excluding a gradual increase in the number of autophagous structures. Moreover, it was concluded that the magnetite nanoparticles synthesized in the presence of different modifiers interact similarly with the cell surface and enter cells by endocytosis.

## Data availability

The data and material generated during and/or analyzed during the current study are available from the corresponding author on reasonable request.

Received: 22 November 2022; Accepted: 6 May 2023

Published online: 15 May 2023

## References

- Martins, P. M., Lima, A. C., Ribeiro, S., Lanceros-Mendez, S. & Martins, P. Magnetic nanoparticles for biomedical applications: from the soul of the earth to the deep history of ourselves. *ACS Appl. Bio Mater.* <https://doi.org/10.1021/acsabm.1c00440> (2021).
- Materón, E. M. *et al.* Magnetic nanoparticles in biomedical applications: A review. *Appl. Surf. Sci. Adv.* <https://doi.org/10.1016/j.apsadv.2021.100163> (2021).
- Roca, A. G. *et al.* Design strategies for shape-controlled magnetic iron oxide nanoparticles. *Adv. Drug Deliv. Rev.* <https://doi.org/10.1016/j.addr.2018.12.008> (2019).
- Ferjaoui, Z. *et al.* Doxorubicin-loaded thermoresponsive superparamagnetic nanocarriers for controlled drug delivery and magnetic hyperthermia applications. *ACS Appl. Mater. Interfaces* <https://doi.org/10.1021/acsami.9b10444> (2019).
- Zheltova, V. *et al.*  $\text{Fe}_3\text{O}_4$ @HAP core-shell nanoparticles as MRI contrast agent: Synthesis, characterization and theoretical and experimental study of shell impact on magnetic properties. *Appl. Surf. Sci.* <https://doi.org/10.1016/j.apsusc.2020.147352> (2020).
- Shete, P. B. *et al.* Magnetic chitosan nanocomposite for hyperthermia therapy application: Preparation, characterization and in vitro experiments. *Appl. Surf. Sci.* <https://doi.org/10.1016/j.apsusc.2013.09.169> (2014).
- Marcu, A. *et al.* Magnetic iron oxide nanoparticles as drug delivery system in breast cancer. *Appl. Surf. Sci.* <https://doi.org/10.1016/j.apsusc.2013.02.072> (2013).
- Govan, J. & Gun'ko, Y. K. Recent advances in the application of magnetic nanoparticles as a support for homogeneous catalysts. *Nanomaterials* <https://doi.org/10.3390/nano4020222> (2014).
- Almomani, F., Bhosale, R., Khraisheh, M., Kumar, A. & Almomani, T. Heavy metal ions removal from industrial wastewater using magnetic nanoparticles (MNP). *Appl. Surf. Sci.* <https://doi.org/10.1016/j.apsusc.2019.144924> (2020).
- Radoń, A., Łukowiec, D. & Włodarczyk, P. Microwave absorption by dextrin-magnetite nanocomposite in frequencies below 2.5 GHz: Role of magnetite content, shape and temperature on magneto-dielectric properties. *Mater. Des.* <https://doi.org/10.1016/j.matdes.2020.108860> (2020).
- Tipsawat, P. *et al.* Magnetite ( $\text{Fe}_3\text{O}_4$ ) nanoparticles: Synthesis, characterization and electrochemical properties. *Appl. Surf. Sci.* **446**, 287–292 (2018).
- Radoń, A., Drygała, A., Hawelek, Ł. & Łukowiec, D. Structure and optical properties of  $\text{Fe}_3\text{O}_4$  nanoparticles synthesized by coprecipitation method with different organic modifiers. *Mater. Charact.* **131**, 148–156 (2017).
- Gavilán, H. *et al.* How size, shape and assembly of magnetic nanoparticles give rise to different hyperthermia scenarios. *Nanoscale* <https://doi.org/10.1039/d1nr03484g> (2021).
- Dheyab, M. A. *et al.* Simple rapid stabilization method through citric acid modification for magnetite nanoparticles. *Sci. Rep.* <https://doi.org/10.1038/s41598-020-67869-8> (2020).
- Favela-Camacho, S. E., Samaniego-Benítez, E. J., Godínez-García, A., Avilés-Arellano, L. M. & Pérez-Robles, J. F. How to decrease the agglomeration of magnetite nanoparticles and increase their stability using surface properties. *Colloids Surf. A Physicochem. Eng. Asp.* <https://doi.org/10.1016/j.colsurfa.2019.04.016> (2019).
- Abdullah, M. M. S. *et al.* Green synthesis of hydrophobic magnetite nanoparticles coated with plant extract and their application as petroleum oil spill collectors. *Nanomaterials* <https://doi.org/10.3390/nano8100855> (2018).
- Rajan, A. & Sahu, N. K. Hydrophobic-to-hydrophilic transition of  $\text{Fe}_3\text{O}_4$  nanorods for magnetically induced hyperthermia. *ACS Appl. Nano Mater.* <https://doi.org/10.1021/acsanm.1c00274> (2021).
- Gorospa, A. E. B., Buenviaje, S. C., Edañol, Y. D. G., Cervera, R. B. M. & Payawan, L. M. One-step co-precipitation synthesis of water-stable poly(ethylene glycol)-coated magnetite nanoparticles. *J. Phys. Conf. Ser.* <https://doi.org/10.1088/1742-6596/1191/1/012059> (2019).
- Maity, D., Chandrasekharan, P., Si-Shen, F., Xue, J. M. & Ding, J. Polyol-based synthesis of hydrophilic magnetite nanoparticles. *J. Appl. Phys.* <https://doi.org/10.1063/1.3355898> (2010).

20. Songvorawit, N., Tuitemwong, K. & Tuitemwong, P. Single step synthesis of amino-functionalized magnetic nanoparticles with polyol technique at low temperature. *ISRN Nanotechnol.* <https://doi.org/10.5402/2011/483129> (2011).
21. Zhang, B. *et al.* Well-defined 3-Aminopropyltriethoxysilane functionalized magnetite nanoparticles and their adsorption performance for partially hydrolyzed polyacrylamide from aqueous solution. *Colloids Surf. A Physicochem. Eng. Asp.* <https://doi.org/10.1016/j.colsurfa.2019.124288> (2020).
22. Akkurt, N., Altan, C. L. & Sarac, M. F. Continuous flow-assisted polyol synthesis of citric acid functionalized iron oxide nanoparticles. *J. Supercond. Nov. Magn.* <https://doi.org/10.1007/s10948-021-06132-1> (2022).
23. Ganapathe, L. S., Mohamed, M. A., Yunus, R. M. & Berhanuddin, D. D. Magnetite (Fe<sub>3</sub>O<sub>4</sub>) nanoparticles in biomedical application: From synthesis to surface functionalisation. *Magnetochemistry* <https://doi.org/10.3390/magnetochemistry6040068> (2020).
24. Włodarczyk, A., Gorgoń, S., Radoń, A. & Bajdak-Rusinek, K. Magnetite nanoparticles in magnetic hyperthermia and cancer therapies: Challenges and perspectives. *Nanomaterials* **12**, 1807 (2022).
25. Xie, Y. *et al.* Size-dependent cytotoxicity of Fe<sub>3</sub>O<sub>4</sub> nanoparticles induced by biphasic regulation of oxidative stress in different human hepatoma cells. *Int. J. Nanomedicine* <https://doi.org/10.2147/IJN.S105575> (2016).
26. Malhotra, N. *et al.* Potential toxicity of iron oxide magnetic nanoparticles: A review. *Molecules* <https://doi.org/10.3390/molecules25143159> (2020).
27. Zhu, N. *et al.* Surface modification of magnetic iron oxide nanoparticles. *Nanomaterials* <https://doi.org/10.3390/nano8100810> (2018).
28. Suk, J. S., Xu, Q., Kim, N., Hanes, J. & Ensign, L. M. PEGylation as a strategy for improving nanoparticle-based drug and gene delivery. *Adv. Drug Deliv. Rev.* <https://doi.org/10.1016/j.addr.2015.09.012> (2016).
29. Abakumov, M. A. *et al.* Toxicity of iron oxide nanoparticles: Size and coating effects. *J. Biochem. Mol. Toxicol.* <https://doi.org/10.1002/jbt.22225> (2018).
30. Shen, L., Li, B. & Qiao, Y. Fe<sub>3</sub>O<sub>4</sub> nanoparticles in targeted drug/gene delivery systems. *Materials* <https://doi.org/10.3390/ma11020324> (2018).
31. Lotfi, S., Ghaderi, F., Bahari, A. & Mahjoub, S. Preparation and characterization of magnetite-chitosan nanoparticles and evaluation of their cytotoxicity effects on MCF7 and fibroblast cells. *J. Supercond. Nov. Magn.* <https://doi.org/10.1007/s10948-017-4094-5> (2017).
32. Liu, Y. *et al.* Characterization of superparamagnetic iron oxide nanoparticle-induced apoptosis in PC12 cells and mouse hippocampus and striatum. *Toxicol. Lett.* <https://doi.org/10.1016/j.toxlet.2018.04.033> (2018).
33. Paunovic, J., Vucevic, D., Radosavljevic, T., Mandić-Rajčević, S. & Pantic, I. Iron-based nanoparticles and their potential toxicity: Focus on oxidative stress and apoptosis. *Chem. Biol. Interact.* <https://doi.org/10.1016/j.cbi.2019.108935> (2020).
34. Zhu, M. T. *et al.* Oxidative stress and apoptosis induced by iron oxide nanoparticles in cultured human umbilical endothelial cells. *J. Nanosci. Nanotechnol.* <https://doi.org/10.1166/jnn.2010.2488> (2010).
35. Roacho-Pérez, J. A. *et al.* Magnetite nanoparticles coated with PEG 3350-Tween 80: In vitro characterization using primary cell cultures. *Polymers (Basel)*. <https://doi.org/10.3390/polym12020300> (2020).
36. Cheraghipour, E., Tamaddon, A. M., Javadpour, S. & Bruce, I. J. PEG conjugated citrate-capped magnetite nanoparticles for biomedical applications. *J. Magn. Magn. Mater.* <https://doi.org/10.1016/j.jmmm.2012.09.042> (2013).
37. He, Q., Wu, Z. & Huang, C. Dual gas-bubble-assisted solvothermal synthesis of magnetite with tunable size and structure. *J. Nanosci. Nanotechnol.* <https://doi.org/10.1166/jnn.2011.4956> (2011).
38. Singh, H. *et al.* Elucidation of the role of hexamine and other precursors in the formation of magnetite nanorods and their stoichiometry. *Phys. Chem. Chem. Phys.* <https://doi.org/10.1039/b917407a> (2010).
39. Rost-Roszkowska, M. *et al.* Influence of soil contaminated with cadmium on cell death in the digestive epithelium of soil centipede *Lithobius forficatus* (Myriapoda, Chilopoda). *Eur. Zool. J.* <https://doi.org/10.1080/24750263.2020.1757168> (2020).
40. Rost-Roszkowska, M. *et al.* Effects of cadmium on mitochondrial structure and function in different organs: studies on the soil centipede *Lithobius forficatus* (Myriapoda, Chilopoda). *Eur. Zool. J.* <https://doi.org/10.1080/24750263.2021.1912199> (2021).
41. Rost-Roszkowska, M. *et al.* Hazards related to the presence of cadmium in food – Studies on the European soil centipede. *Lithobius forficatus*. *Sci. Total Environ.* **845**, 157298 (2022).
42. Rebhi, A., Makhlouf, T. & Njah, N. X-Ray diffraction analysis of 99.1% recycled aluminium subjected to equal channel angular extrusion. *Phys. Proc.* **2**, 1263–1270 (2009).
43. Patel, C. M., Chakraborty, M. & Murthy, Z. V. P. Study on the stability and microstructural properties of barium sulfate nanoparticles produced by nanomilling. *Adv. Powder Technol.* **25**, 226–235 (2014).
44. Radoń, A., Hawelek, I., Łukowicz, D., Kubacki, J. & Włodarczyk, P. Dielectric and electromagnetic interference shielding properties of high entropy (Zn, Fe, Ni, Mg, Cd)Fe<sub>2</sub>O<sub>4</sub> ferrite. *Sci. Rep.* <https://doi.org/10.1038/s41598-019-56586-6> (2019).
45. Iqbal, Y., Bae, H., Rhee, I. & Hong, S. Relaxivities of hydrogen protons in aqueous solutions of PEG-coated rod-shaped manganese-nickel-ferrite (Mn<sub>0.4</sub>Ni<sub>0.6</sub>Fe<sub>2</sub>O<sub>4</sub>) nanoparticles. *J. Korean Phys. Soc.* <https://doi.org/10.3938/jkps.65.1594> (2014).
46. Khairuddin, A. B. *et al.* FTIR studies on the effect of concentration of polyethylene glycol on polymerization of Shellac. *J. Phys. Conf. Ser.* <https://doi.org/10.1088/1742-6596/776/1/012053> (2016).
47. Röska, B. *et al.* Determination of the hydrogen-bond network and the ferrimagnetic structure of a rockbridgeite-type compound, Fe<sup>2+</sup>Fe<sup>3+</sup><sub>3/2</sub>(Mn<sup>2+</sup>Zn)<sub>0.8</sub>(PO<sub>4</sub>)<sub>3</sub>(OH)<sub>4.2</sub>(HOH)<sub>0.8</sub>. *J. Phys. Condens. Matter* <https://doi.org/10.1088/1361-648X/aac0cd> (2018).
48. Alemdar, A., Güngör, N., Ece, O. I. & Atici, O. The rheological properties and characterization of bentonite dispersions in the presence of non-ionic polymer PEG. *J. Mater. Sci.* <https://doi.org/10.1007/s10853-005-5703-4> (2005).
49. Dreyfuss, J. M., Jones, S. B. & Sayedy, Y. Hexamethylenetetramine: A Review. *Am. Ind. Hyg. Assoc. J.* <https://doi.org/10.1080/15298668991375191> (1989).
50. Kaszuba, M., Corbett, J., Watson, F. M. N. & Jones, A. High-concentration zeta potential measurements using light-scattering techniques. *Philos. Trans. R. Soc. A Math. Phys. Eng. Sci.* <https://doi.org/10.1098/rsta.2010.0175> (2010).
51. Abdellahi, M., Tajally, M. & Mirzaee, O. A mathematical-physical model to compare the heating potential of the ferromagnetic and superparamagnetic nanoparticles. *Chin. J. Phys.* <https://doi.org/10.1016/j.cjph.2021.12.033> (2022).
52. Kafrouni, L. & Savadogo, O. Recent progress on magnetic nanoparticles for magnetic hyperthermia. *Prog. Biomater.* **5**, 147–160 (2016).
53. Pucci, C., Degl'Innocenti, A., Belenli Gümüş, M. & Ciofani, G. Superparamagnetic iron oxide nanoparticles for magnetic hyperthermia: Recent advancements, molecular effects, and future directions in the omics era. *Biomater. Sci.* **10**, 2103–2121 (2022).
54. Jose, J. *et al.* Magnetic nanoparticles for hyperthermia in cancer treatment: an emerging tool. *Environ. Sci. Pollut. Res.* <https://doi.org/10.1007/s11356-019-07231-2> (2020).
55. Kouzoudis, D., Samourkanidis, G., Kolokithas-Ntoukas, A., Zoppellaro, G. & Spiliotopoulos, K. Magnetic hyperthermia in the 400–1,100 kHz frequency range using MIONs of condensed colloidal nanocrystal clusters. *Front. Mater.* <https://doi.org/10.3389/fmats.2021.638019> (2021).
56. Lanier, O. L. *et al.* Evaluation of magnetic nanoparticles for magnetic fluid hyperthermia. *Int. J. Hyperth.* <https://doi.org/10.1080/02656736.2019.1628313> (2019).
57. Kallumadil, M. *et al.* Suitability of commercial colloids for magnetic hyperthermia. *J. Magn. Magn. Mater.* <https://doi.org/10.1016/j.jmmm.2009.02.075> (2009).
58. Carrey, J., Mehdaoui, B. & Respaud, M. Simple models for dynamic hysteresis loop calculations of magnetic single-domain nanoparticles: Application to magnetic hyperthermia optimization. *J. Appl. Phys.* <https://doi.org/10.1063/1.3551582> (2011).



59. Rosensweig, R. E. Heating magnetic fluid with alternating magnetic field. *J. Magn. Magn. Mater.* [https://doi.org/10.1016/S0304-8853\(02\)00706-0](https://doi.org/10.1016/S0304-8853(02)00706-0) (2002).
60. Obaidat, I. M., Narayanaswamy, V., Alaabed, S., Sambasivam, S. & Muralee Gopi, C. V. V. Principles of magnetic hyperthermia: A focus on using multifunctional hybrid magnetic nanoparticles. *Magnetochemistry* <https://doi.org/10.3390/magnetochemistry5040067> (2019).
61. Conde-Leboran, I. *et al.* A single picture explains diversity of hyperthermia response of magnetic nanoparticles. *J. Phys. Chem. C* <https://doi.org/10.1021/acs.jpcc.5b02555> (2015).
62. Kim, J., Wang, J., Kim, H. & Bae, S. Concentration-dependent oscillation of specific loss power in magnetic nanofluid hyperthermia. *Sci. Rep.* <https://doi.org/10.1038/s41598-020-79871-1> (2021).
63. Deatsch, A. E. & Evans, B. A. Heating efficiency in magnetic nanoparticle hyperthermia. *J. Magn. Magn. Mater.* <https://doi.org/10.1016/j.jmmm.2013.11.006> (2014).
64. Abu-Bakr, A. F. & Zubarev, A. Y. Effect of ferromagnetic nanoparticles aggregation on magnetic hyperthermia. *Eur. Phys. J. Spec. Top.* <https://doi.org/10.1140/epjst/e2019-900027-6> (2020).
65. Guibert, C., Dupuis, V., Peyre, V. & Fresnais, J. Hyperthermia of magnetic nanoparticles: experimental study of the role of aggregation. *J. Phys. Chem. C* <https://doi.org/10.1021/acs.jpcc.5b07796> (2015).
66. Gneveckow, U. *et al.* Description and characterization of the novel hyperthermia- and thermoablation-system MFH<sup>®</sup>300F for clinical magnetic fluid hyperthermia. *Med. Phys.* <https://doi.org/10.1118/1.1748629> (2004).
67. Khan, A. S., Nasir, M. F., Khan, M. T., Murtaza, A. & Hamayun, M. A. Study of structural, magnetic and radio frequency heating aptitudes of pure and (Fe-III) doped manganite (La<sub>1-x</sub>Sr<sub>x</sub>MnO<sub>3</sub>) and their incorporation with sodium poly-styrene sulfonate (PSS) for magnetic hyperthermia applications. *Phys. B Condens. Matter* <https://doi.org/10.1016/j.physb.2020.412627> (2021).
68. Atkinson, W. J., Brezovich, I. A. & Chakraborty, D. P. Usable frequencies in hyperthermia with thermal seeds. *IEEE Trans. Biomed. Eng.* <https://doi.org/10.1109/TBME.1984.325372> (1984).
69. Hergt, R. & Dutz, S. Magnetic particle hyperthermia-biophysical limitations of a visionary tumour therapy. *J. Magn. Magn. Mater.* <https://doi.org/10.1016/j.jmmm.2006.10.1156> (2007).
70. Bellizzi, G. & Bucci, O. M. On the optimal choice of the exposure conditions and the nanoparticle features in magnetic nanoparticle hyperthermia. *Int. J. Hyperth.* <https://doi.org/10.3109/02656730903514685> (2010).
71. Bellizzi, G., Bucci, O. M. & Chirico, G. Numerical assessment of a criterion for the optimal choice of the operative conditions in magnetic nanoparticle hyperthermia on a realistic model of the human head. *Int. J. Hyperth.* <https://doi.org/10.3109/02656736.2016.1167258> (2016).
72. Tsiapla, A. R. *et al.* Mitigation of magnetic particle hyperthermia side effects by magnetic field controls. *Int. J. Hyperth.* <https://doi.org/10.1080/02656736.2021.1899310> (2021).
73. Yang, R. *et al.* Effect of Mg doping on magnetic induction heating of Zn-Co ferrite nanoparticles. *J. Alloys Compd.* <https://doi.org/10.1016/j.jallcom.2020.156907> (2021).
74. Wang, Z., Deng, Q., Wang, Z. & Chong, T. Effects of autophagy on the proliferation and apoptosis of clear cell renal carcinoma 786-O cells. *Int. J. Clin. Exp. Pathol.* **12**, 1342–1349 (2019).
75. Yun, H. R. *et al.* Roles of autophagy in oxidative stress. *Int. J. Mol. Sci.* <https://doi.org/10.3390/ijms21093289> (2020).
76. Liu, J., Dai, C. & Hu, Y. Aqueous aggregation behavior of citric acid coated magnetite nanoparticles: Effects of pH, cations, anions, and humic acid. *Environ. Res.* <https://doi.org/10.1016/j.envres.2017.10.045> (2018).
77. Corbo, C. *et al.* The impact of nanoparticle protein corona on cytotoxicity, immunotoxicity and target drug delivery. *Nanomedicine* <https://doi.org/10.2217/nnm.15.188> (2016).
78. Zaffaroni, N. & Beretta, G. L. Nanoparticles for ferroptosis therapy in cancer. *Pharmaceutics* <https://doi.org/10.3390/pharmaceutics13111785> (2021).
79. Chen, R. J. *et al.* The current understanding of autophagy in nanomaterial toxicity and its implementation in safety assessment-related alternative testing strategies. *Int. J. Mol. Sci.* <https://doi.org/10.3390/ijms21072387> (2020).
80. Li, Y. & Ju, D. The role of autophagy in nanoparticles-induced toxicity and its related cellular and molecular mechanisms. *Adv. Exp. Med. Biol.* [https://doi.org/10.1007/978-3-319-72041-8\\_5](https://doi.org/10.1007/978-3-319-72041-8_5) (2018).
81. Lin, P. W., Chu, M. L. & Liu, H. S. Autophagy and metabolism. *Kaohsiung J. Med. Sci.* <https://doi.org/10.1002/kjm2.12299> (2021).
82. Alili, L. *et al.* Effect of Fe<sub>3</sub>O<sub>4</sub> nanoparticles on skin tumor cells and dermal fibroblasts. *Biomed. Res. Int.* <https://doi.org/10.1155/2015/530957> (2015).

## Acknowledgements

This work was supported by the internal source: Łukasiewicz Research Network—Institute of Non-Ferrous Metals own studies, report no. 8163/21.

## Author contributions

A.R., A.W., M.R.-R., Ł.S. and Ł.C. developed the methodology. A.R. and A.C. synthesized the nanoparticles and performed magnetic hyperthermia measurements. A.R., A.K.-B., and D.Ł. analyzed the structure and morphology of nanoparticles. S.W. measured and analyzed the hydrodynamic size and zeta potential. A.W. and Ł.S. performed and analyzed toxicology tests on dermal fibroblasts. M.R.-R. and Ł.C. collected and analyzed TEM images of fibroblast cells. A.R. and A.W. wrote the main manuscript text. P.G. performed and analyzed the magnetic properties of nanoparticles. A.K.-B. supervised research works. All authors reviewed and approved the manuscript.

## Competing interests

The authors declare no competing interests.

## Additional information

**Supplementary Information** The online version contains supplementary material available at <https://doi.org/10.1038/s41598-023-34738-z>.

**Correspondence** and requests for materials should be addressed to A.R.

**Reprints and permissions information** is available at [www.nature.com/reprints](http://www.nature.com/reprints).

**Publisher's note** Springer Nature remains neutral with regard to jurisdictional claims in published maps and institutional affiliations.



**Open Access** This article is licensed under a Creative Commons Attribution 4.0 International License, which permits use, sharing, adaptation, distribution and reproduction in any medium or format, as long as you give appropriate credit to the original author(s) and the source, provide a link to the Creative Commons licence, and indicate if changes were made. The images or other third party material in this article are included in the article's Creative Commons licence, unless indicated otherwise in a credit line to the material. If material is not included in the article's Creative Commons licence and your intended use is not permitted by statutory regulation or exceeds the permitted use, you will need to obtain permission directly from the copyright holder. To view a copy of this licence, visit <http://creativecommons.org/licenses/by/4.0/>.

© The Author(s) 2023